Detection and Mitigation of Electrostatic Pull-in Instability in MEMS Parallel Plate Actuators

by

Colin Stevens

A dissertation submitted to the Graduate Faculty of
Auburn University
in partial fulfillment of the
requirements for the Degree of
Doctor of Philosophy

Auburn, Alabama
August 3, 2013

Keywords: MEMS, Resonator, Parallel Plate Actuator, Pull-in, Current Sensing

Copyright 2013 by Colin Stevens

Approved by

Dr. Robert N. Dean, Chair, Associate Professor of Electrical and Computer Engineering
Dr. Thaddeus Roppel, Associate Professor of Electrical and Computer Engineering
Dr. Thomas Baginski, Professor of Electrical and Computer Engineering
Dr. Vishwani Agrawal, Professor of Electrical and Computer Engineering
Dr. Darren Olsen, Assistant Professor of Architecture, Design and Construction

Abstract

Electrostatic MEMS actuators are used in a wide variety of applications including micro-machined gyroscopes, high speed mechanical switches, variable capacitors, and vibration isolation devices. MEMS parallel plate actuators (PPAs) are simple to realize, yet complex nonlinear variable capacitors. If a DC voltage is applied in an attempt to move the proof mass greater than 1/3 of the electrode rest gap distance, the device becomes unstable and the electrodes snap into contact. Most research into this pull-in phenomenon is devoted to extending the operational range of motion past the 1/3 instability point. This usually involves the addition of complex external electronics. Many electronics applications, however, only require that the actuator remain out of the pull-in region, and do not require an extended stable range of motion. If detection of the pull-in event is all that is required, then simpler solutions can be realized, minimizing the requirements on the driving signal. Once pull-in is reached, the velocity of the movable plate increases rapidly until the plates make contact. The decreasing distance causes a proportional increase in capacitance. To maintain a constant voltage across the plates, an inrush of current must flow into the actuator in response to the increased capacitance. This work presents a method for detecting the inrush current using a transimpedance amplifier circuit to convert the current to a measurable voltage. Once pull-in is detected, the PPA is electrically shutdown to prevent damage to the actuator or the voltage source, thus mitigating pull-in. A simulation of the expected results was performed using a Simulink model for the actuator structure predicting the expected range of inrush current. This result was then verified using a silicon micro-machined PPA connected to the detection/mitigation circuit on a Printed Circuit Board (PCB). The experimental results follow closely with the simulation allowing precise control in mitigating the pull-in event.

Table of Contents

Abstract ii

List of Figures vi

List of Tables ix

Acknowledgements x

1 Introduction 1

2 Mathematical Theory and Motivation 3

2.1 Parallel Plate Actuator Overview 3

2.1.1 Derivation of Electric Field of A Parallel Plate Capacitor 3

2.1.2 Derivation of Force Equations of a Parallel Plate Actuator 7

2.1.3 Stability Points For the PPA 10

2.2 Motivation 15

2.2.1 Disadvantages of Pull-In 16

2.2.2 Advantages of Pull-in 17

2.3 Chapter Summary 18

3 Literature Review 20

3.1 MEMS Devices that Make Use of Pull-in 20

3.2 Actuator Control 21

3.3 Chapter Summary 24

4 Theory Development of Pull-In Sensing Mechanism 25

4.1 Current Sensing 25

4.1.1 High Side Current Sensing 25

4.1.2 Low Side Current Sensing 28

4.1.3 Low-Side Transimpedance Amplification Sensing 29

4.2 Hall Effect Sensing 30
4.3 Optical Sensing 31
4.4 Piezoresistive Sensing 31
4.5 Secondary Capacitance 32
4.6 Current Transformer 32
4.7 Chapter Summary 33
5 PPA Design and Fabrication 35
5.1 Intellisuite Simulation of PPA device 35
5.2 Simulink Simulation Pull-in Detection Operation 37
5.3 Fabrication Equipment and Processing 42
5.3.1 Cleaning Equipment and Processes 42
5.3.2 Patterning Equipment 46
5.3.3 Silicon Processing Equipment 50
5.4 Plasma Assisted Dry Etching of Silicon 51
5.4.1 Plasma Etching 51
5.4.2 Reactive Ion Etching 52
5.4.3 Inductive Coupling of Plasma 53
5.4.4 Deep Reactive Ion Etching 53
5.4.5 Electron Beam Evaporation and Sputtering System 57
5.4.6 Masking Materials 58
5.4.7 Silicon Oxidation 59
5.5 Chapter Summary 60
6 Experimental Verification of Pull-in Detection and Mitigation 61
6.1 Schematic and Layout of Test Platform 62
6.2 Results of Test Platform Measurement 68
6.3 Chapter Summary 73
7 Extension of Pull-in Work to Create a Tunable Resonator 75

7.1 Pull-in Resonator 75
7.2 Pull-in Resonator Simulation 78
7.3 Pull-in resonator Experimental Verification 80
7.4 Chapter Summary 86
8 Conclusions 88
9 Future Work 90
9.1 Pull-in Detection Future Work 90
9.2 Pull-in Resonator Future Work 91
Bibliography 92

Appendices 97

A PPA Traveller 98
B Electron Beam Metal Deposition 102
C Listing of Lab Equipment by Room#/Laboratory 103
D Matlab Code used to Analyze Interferometer Data 105
E Schematic Drawing of PPA Board Mount Fixture 110

List of Figures

2.1 Electric Field Due to a Line Charge. 4

2.2 Electric field due to an infinite sheet of charge. 6

2.3 Visualization of the electric field between two infinite sheets of charge. 7

2.4 Voltage as a function of movable plate displacement from equation 2.33. 12

2.5 Pole Zero map of actuator at different points of stability 15

4.1 Simplified schematic of a high side current sense circuit 27

4.2 Compensation circuit to account for high voltage MEMS devices 28

4.3 Schematic of a low side current sense circuit 29

4.4 Schematic of a transimpedance amplification circuit 30

4.5 Polytech OFV Vibrometer 31

5.1 Intellisuite simulation of PPA structure 36

5.2 Transmissibility of the fabricated PPA 38

5.3 Simulink Model of PPA 40

5.4 Current and Position Results of Simulink PPA Under Ramping Voltage. 41

5.5 Spin Rinse Dryer 45

5.6 Vapor HMDS Application Chamber 47

5.7 Photoresist Spinner 48

5.8 Matrix Oxygen Plasma Asher 49

5.9 [Karl Suss MA/BA6 Contact Mask Aligner 50

5.10 STS Advanced Silicon Etcher 54

5.11 Oxidation Furnace 57

5.12 CHA Mark 50 dual E-beam/sputter/ion gun deposition system 58

6.1 Electrical Schematic of Transimpedance amplifier Pull-in Detection Circuit . . . 64

6.2 Layout of Transimpedance Amplification Circuit. 66

6.3 Fabricated Transimpedance Amplification Circuit. 67

6.4 Pull-in Event Without Safety Shutdown. 69

6.5 Safety Shutdown at 4.88e-7 Amps. 72

6.6 PSafety Shutdown at 8.82e-7 Amps. 73

7.1 Mass Spring Damper System Diagram. 76

7.2 Actuator Circuit. 77

7.3 Simulink Model Using 4M Resistance. 79

7.4 Simulink Model Using 8M Resistance. 80

7.5 PCB Electrode. 82

7.6 Fabricated PPA Spring System. 82

7.7 Assembled PPA test device. 83

7.8 Pull-in Oscillations at Various Resistances. 84

7.9 FFT Analysis of Pull-in Data 85

7.10 Frequency Trend as a Function of Resistance. 86

E.1 Bottom of fixture Design. 110

E.2 Top of fixture Design. 111

List of Tables

5.1 Intellisuite modal simulation of designed PPA device. 36

5.2 Parallel Plate Actuator Device Properties 39

5.3 Simulink Analysis of Current as a Function of PPA Position 42

5.4 RCA Process 43

5.5 MORGNSOI DRIE Recipe 56

6.1 Experimental Analysis of Current as a Function of Position 70

B.1 Electron Beam Metal Deposition Recipe 102

Acknowledgements

I would like to thank Dr. Robert Dean for offering his guidance in my graduate curriculum, as well as his valuable input on this project, and Mr. Charles Ellis for lending his expertise in the many areas that I had no knowledge. I would like to thank my father William Stevens, my mother, Martha Stevens, and my sister, Kristen Fink for their encouragement and support. I would also like to thank my co-workers in the AT&T engineering department for their encouragement to return to college and pursue my graduate education.

Chapter 1

Introduction

MEMS parallel plate actuators are a commonly used type of electrostatic actuator that have applications in a number of different kinds of micro-machined devices, including RF devices [1], variable capacitors [2], accelerometers [3], micro-mirrors, and active vibration isolators [4]. One issue that is inherent to all parallel plate actuators (PPA) is the condition of pull-in. Pull-in is the inability of a PPA to be electrostatically actuated beyond one third of its rest gap distance without becoming unstable. Most PPA devices in widespread use are designed so that they only operate while in an open-loop stable range of motion. These devices must be designed so that they are not actuated beyond this point unless additional circuity is added to prevent pull-in from occurring.

Two of the driving factors in MEMS production today is the reduction of size and cost. Many of the current systems in place to prevent pull-in have disadvantages that either increase complexity of the system which can result in both a size and a cost increase, or somehow degrade the performance of the device. If a solution to prevents pull-in from occurring can be found that does not introduce excessive additional electronics to the system or have adverse effects in the operation of the device, then cost as well as size benefits can be realized.

This dissertation introduces the concept of the PPA, presents the theory behind its operation, including the dynamics of motion, and points of instability. A review of the current work being conducted into PPA's to increase the efficiency of motion is investigated. A simple but overlooked method of detection of PPA instability is then proposed that has the potential to prevent damage to systems without suffering an increase in cost or complexity of the system. By using a transimpedance amplifier to greatly amplify the current signal

passing through the actuator, a system can be warned of impending instability and take steps to either mitigate or record the event. To justify this proposal, a through simulation of the dynamics of motion is presented, and then verified experimentally.

In addition to the proposed transimpedance amplification solution to detect pull-in by current amplification, introduction of a simple passive resistor to cause a modification of the current can cause an interesting behavior in the dynamics of motion which can cause the device to go into an oscillatory state. This behavior of pull-in can be utilized to create a tunable resonator that relies only on a DC voltage and one passive component. A full implementation of this is presented which can be used in conjunction with the detection method previously discussed.

Chapter 2

Mathematical Theory and Motivation

The following chapter provides the mathematical analysis of the PPA required to understand the operation of the PPA. A derivation of the force equations covered and the concept of pull-in instability is explained. The effects of pull-in are then analyzed to give an understanding of the advantages and disadvantages of the pull-in phenomena and the motivation of this work.

2.1 Parallel Plate Actuator Overview

The parallel plate capacitor can be generally characterized as two parallel infinite sheets of opposite charge located a set distance from each other if fringing fields are neglected.

2.1.1 Derivation of Electric Field of A Parallel Plate Capacitor

The force acting on the capacitor can be found by deriving the equation for the electric field between the two plates, which are also referred to as electrodes, from Coulomb's law. Using the concept of symmetry, the mathematical derivation can be greatly reduced as shown below. By first finding the equation for the electric field at a point due to an infinite line, it is shown that the the components of the electric field vectors that are not normal to the point cancel out. [5]

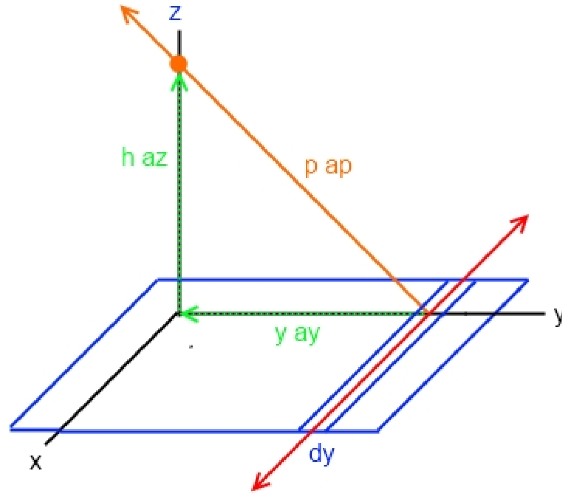

Figure 2.1: Electric Field Due to a Line Charge.

$$\vec{E} = \frac{Q}{4\pi\varepsilon R^2}\hat{a}_r \text{ (Coulomb's law point of charge)} \tag{2.1}$$

In 2.1, $\vec{E}$ is the electric field vector, Q is the charge in coulombs, ε is the permittivity of the material through which the electric field travels, R is the radius from the charge, and $\hat{a}_r$ is the unit vector.

$$dQ = \rho_l dz \tag{2.2}$$

The distance from each of these points $\vec{R}$ has a magnitude R and a unit vector direction that can be expressed in its component form shown in 2.3

$$\vec{R} = R\hat{a}_r = \rho\hat{a}_\rho - z\hat{a}_z \tag{2.3}$$

From equation 2.3 the magnitude and unit vector direction of each dQ can be found in terms of its component vectors shown in 2.4

$$R = \sqrt{\varepsilon^2 + z^2}, \quad \hat{a}_r = \frac{\rho \hat{a}_\rho - z \hat{a}_z}{\sqrt{\varepsilon^2 + z^2}} \tag{2.4}$$

By substituting back into the Coulomb's Law equation, the electric field vector at a point due to each discrete charge density can be found. Then by summing all of the discrete charge densities, the total electric field on the point due to the infinite line can be found as shown in 2.5, 2.6, 2.7.

$$E = \int \frac{\rho_l dz}{4\pi\varepsilon} \frac{\rho \hat{a}_\rho - z \hat{a}_z}{(\rho^2 + z^2)^{\frac{3}{2}}} \tag{2.5}$$

$$E = \frac{\rho_l \rho \hat{a}_\rho}{4\pi\varepsilon} \int_{-\infty}^{+\infty} \frac{dz}{(\rho^2 + z^2)^{\frac{3}{2}}} \tag{2.6}$$

$$\vec{E} = \frac{\rho_l}{2\pi\varepsilon\rho} \widehat{a}_\rho \tag{2.7}$$

The equation for the electric field due to an infinite sheet of charge can then be found by using the previous equation for an infinite line of charge and integrating over an infinite number of lines as shown below. [5]

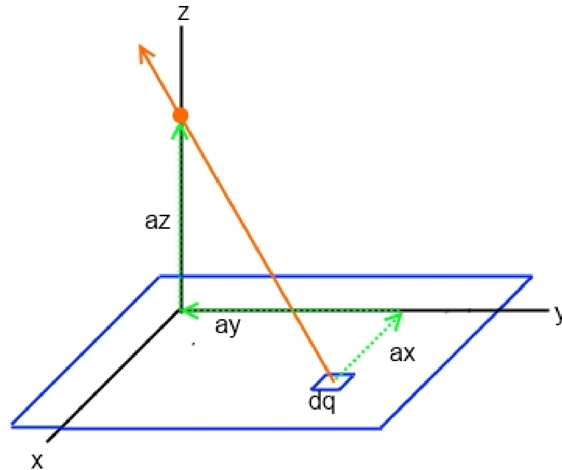

Figure 2.2: Electric field due to an infinite sheet of charge.

Now consider an infinite sheet of charge lying in the x-y plane and a point a distance z normal to the plane. The sheet can be approximated by an infinite sheet of infinitely small charges. Each infinitely small charge can then be approximated by a sheet density ρ_s times infinitely small distances dx and dy shown in equation 2.8.

$$dQ = \rho_s dx dy \tag{2.8}$$

To make things simpler the sheet can also be approximated by an infinite number of infinite lines of charges with charge density ρ_l therefore the substitution in equation 2.9.

$$\rho_l = \rho_s dy \tag{2.9}$$

This reduces the equation down to one integral of infinite lines. By substituting 2.7 and taking the integral shown in 2.10, the equation for the electric field vector at a point due to

an infinite sheet can be obtained in 2.12.

$$\rho a_\rho = -y\hat{a}_{\mathbf{y}} + h\hat{a}_{\mathbf{z}} \tag{2.10}$$

$$E = \frac{\rho_s h\hat{a}_{\mathbf{z}}}{2\pi\varepsilon_o\varepsilon_r}\int_{-\infty}^{+\infty}\frac{dy}{(y^2+h^2)} \tag{2.11}$$

$$E = \frac{\rho_s}{2\varepsilon_o\varepsilon_r}\widehat{a}_z \tag{2.12}$$

From the above equation, it is shown that the electric field is constant at any distance from the surface of the sheet of charge. Because of this, the electric field between two oppositely charged sheets of charge can be found by multiplying this constant value by 2 as shown below.

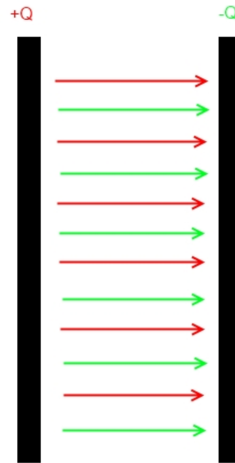

Figure 2.3: Visualization of the electric field between two infinite sheets of charge.

$$E = \frac{\rho_s}{\varepsilon_o\varepsilon_r}\widehat{a}_z \tag{2.13}$$

2.1.2 Derivation of Force Equations of a Parallel Plate Actuator

Using the above equation for the electric field between two infinite sheet charges, the equation for the electrostatic force resulting from this charge can be found by finding the

potential energy created by the work done to bring the two sets of charges to their respective separation distance as shown in 2.15. [5]

$$V = -\int_a^b E \cdot dl = Ed = \frac{qd}{\varepsilon A} = \frac{q}{C} \tag{2.14}$$

Similarly,

$$FdQ = \frac{W}{Q} \tag{2.15}$$

A is the area of the capacitor, C is the capacitance of the capacitor, F is the force between the two plates, W is work, and Q is charge on the capacitor.

$$U_E = \int_0^Q \frac{Q}{C} dq \tag{2.16}$$

By manipulating the equation $Q = CV$ different forms for expressing the potential energy in the capacitor are shown in 2.17

$$U_E = \frac{1}{2}\frac{Q^2}{C} = \frac{1}{2}QV = \frac{1}{2}CV^2 \tag{2.17}$$

The equation for the capacitance of a parallel plate actuator as a function of distance is as follows where ε_o is the permittivity of free space, ε_r is the relative permittivity of the dielectric material, and d is the gap thickness in meters.

$$C(d) = \frac{\varepsilon_o \varepsilon_r A}{d} \tag{2.18}$$

By substituting 2.18 into 2.17 the equation for potential energy as a function of gap thickness.

$$U_E = \frac{1}{2}\frac{\varepsilon_o \varepsilon_r A}{d} V^2 \ (d = \mathit{gap\ thickness}) \tag{2.19}$$

A parallel plate capacitor can be considered a parallel plate actuator with a fixed gap distance by replacing the set gap distance d, with the variable $x_o - x(t)$ in 2.21 , where x_o

is the rest gap distance and x is the variable distance at a given moment. The electrostatic force on the parallel plate electrodes can be found by taking the integral of the potential energy equation shown in 2.22. [6]

$$d\left(t\right) = x_o - x\left(t\right) \tag{2.20}$$

$$U_E\left(t\right) = \frac{1}{2}\frac{\varepsilon_o\varepsilon_r A}{\left(x_o - x\left(t\right)\right)}V^2 \tag{2.21}$$

$$U_E\left(t\right) = \int_C F \cdot \frac{dx}{dt} \tag{2.22}$$

Finally the force on a PPA is then

$$F(t) = \frac{1}{2}\frac{\varepsilon_o\varepsilon_r A}{\left(x_o - x\left(t\right)\right)^2}V^2 \tag{2.23}$$

This force is always an attractive force in which the electrodes always seek to move in a manner that increases capacitance.

The PPA consists of a movable conductive plate suspended over another conductive fixed plate that is clamped on at least two sides by a suspension system that maintain the plate's position at its rest gap distance above the fixed electrode. The suspension system exerts a force on the movable electrode which is defined by hooks law shown in 2.26. As the electrostatic force due to the charge pulls the movable plate in one direction, the reactionary force of the suspension system pushes back in the opposite direction.

$$U_s\left(t\right) = \int_0^x kx\ \frac{dx}{dt} \tag{2.24}$$

$$F(t) = -\frac{dU_s(t)}{dx} \tag{2.25}$$

$$F(t) = -kx(t) \tag{2.26}$$

The net force on the plates is then the sum of the electrostatic force and the spring force.

$$F_{net}(t) = \frac{V^2 \varepsilon_o \varepsilon_r A}{2x_o - x(t)^2} - \ kx(t) \tag{2.27}$$

When the two forces are equal, the net force is zero and the system is in equilibrium; therefore, an equation for position of the actuator can be found with respect to voltage. The resulting equation is a quadratic expression which consists of a stable region where the spring force balances the electrostatic force, and an unstable region where the electrostatic force is dominant. The voltage where these two regions meet is called the pull-in voltage, and can be found by finding the critical point of the equation where the voltage is at its maximum. The voltage attempting to achieve a displacement of $\frac{x_o}{3}$ or greater, the spring force is no longer able to withstand the electrostatic force and the electrodes will respond in an unstable manner and accelerate into physical contact. This unstable reaction is called pull-in. The pull-in voltage can then be found by substituting this position into the value x of the original expression shown in 2.30. [7]

$$kx(t) = \frac{V^2 \varepsilon_o \varepsilon_r A}{2x_o - x(t)^2} \tag{2.28}$$

$$\frac{x_o}{3} = x(t) \tag{2.29}$$

$$\mathrm{V_p} = \sqrt{\frac{8}{27} \frac{\mathrm{kx_o^3}}{\varepsilon \mathrm{A}}} \tag{2.30}$$

2.1.3 Stability Points For the PPA

An analysis of the stability of the PPA can be performed by finding the the pole locations of the system as electrostatic voltage is applied to the system. To account for the dynamic motion in one direction, the mass spring system can be modeled as a second order differential

equation as shown in figure 2.31

$$m\ddot{x} + c\dot{x} + kx = f(t) = \frac{\varepsilon A V^2}{2(x_o - x(t))^2} \tag{2.31}$$

At equilibrium:

$$kx = \frac{\varepsilon A V^2}{2(x_o - x(t))^2} \tag{2.32}$$

and this equation can be used to find an expression for V as a function of displacement, x, which is illustrated in figure 2.4:

$$V = \sqrt{\frac{2(x_o - x(t))^2}{\varepsilon A}} \tag{2.33}$$

The graph in figure 2.4 represents the voltage on the PPA as a function of PPA displacement distance. As the graph shows, the voltage required to maintain a stable position increases as the plate moves further from its nominal gap and toward the opposing plate. When the plate reaches one-third of the full distance, the required stable voltage reaches a maximum. Beyond this position, the force due to voltage becomes greater than the opposing spring force, causing the equivalent voltage to decrease. Using a fixed voltage source, the system has no way to compensate for the decreased voltage requirement to maintain a stable position, thus causing the plates to pull together completely. [8]

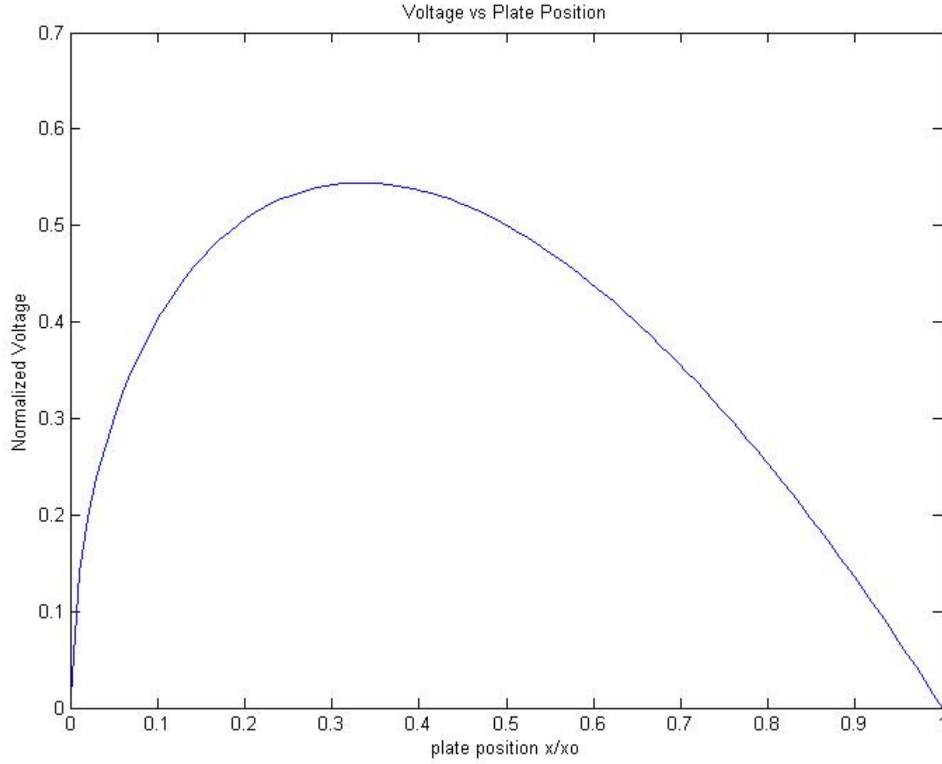

Figure 2.4: Voltage as a function of movable plate displacement from equation 2.33.

Over the stable operating range ($0 \leq x \leq x_o/3$), equation (2.33) and a Taylor's series expansion for f(t) about x can be used to develop a linearized model of the electrostatic spring effect in order to evaluate the effect on the poles.

For the Taylor series:

$$f'(f(t)) = \frac{\varepsilon A V^2}{(x_o - x(t))^3} \tag{2.34}$$

Let x_a be a desired displacement over the stable range and V_a be the voltage from (2.33). Therefore:

$$f(t) \approx \frac{\frac{\varepsilon A V_a^2}{2(x_o - x_a)^2}}{0!}(x(t) - x_a)^0 + \frac{\frac{\varepsilon A V_a^2}{(x_o - x_a)^3}}{1!}(x(t) - x_a)^1 = N + k_{EL}x(t) \tag{2.35}$$

$$m\ddot{x} + c\dot{x} + (k - k_{EL})x = N \tag{2.36}$$

which is only valid at the particular values of V_a and x_a. From the quadratic formula, the pole locations are:

$$poles = \frac{\frac{-c}{m} + \sqrt{\frac{c}{m}^2 - 4\frac{k-k_{EL}}{m}}}{2} \tag{2.37}$$

Using (2.33), (2.35) and (2.37), an s-plane map of the poles for system between x = 0 and x = $x_o/3$ can be obtained. This map is shown below in Figure 2.5

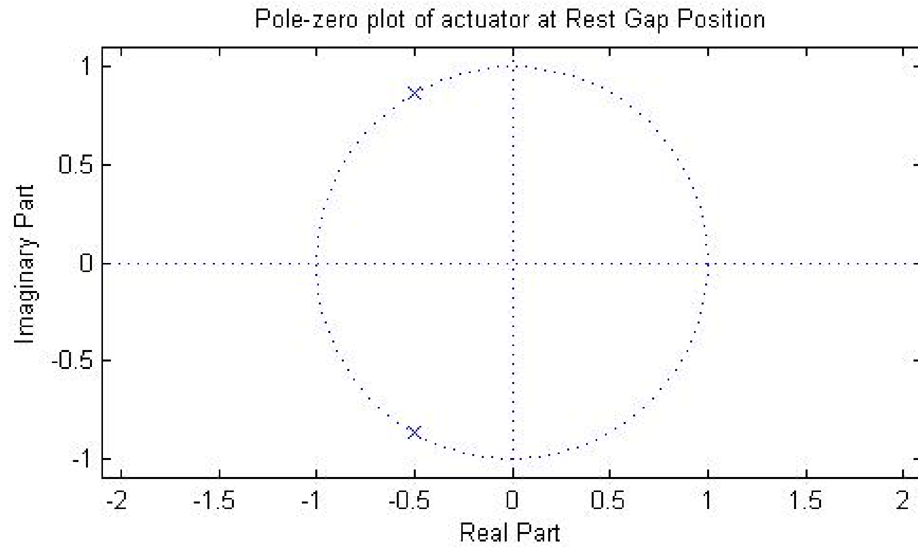

(a) Rest Gap Position

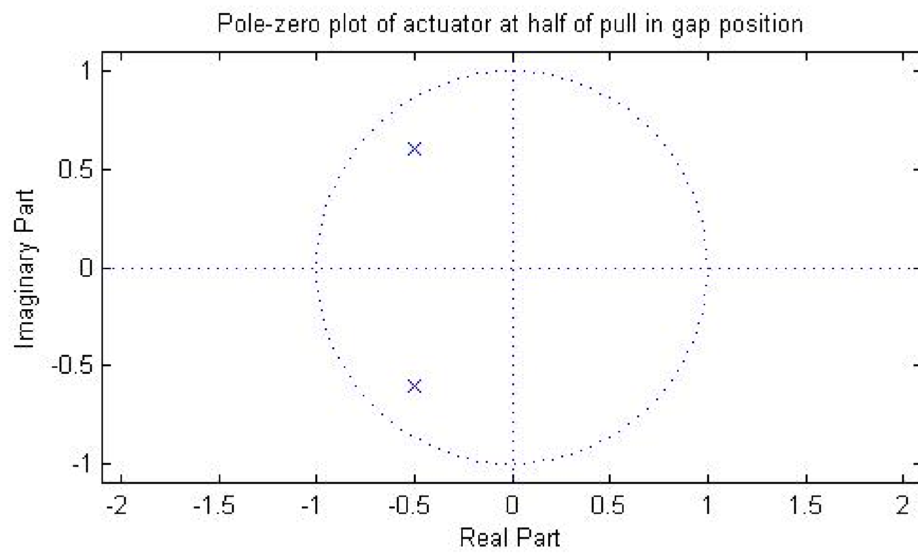

(b) 1/2 of pull in Position

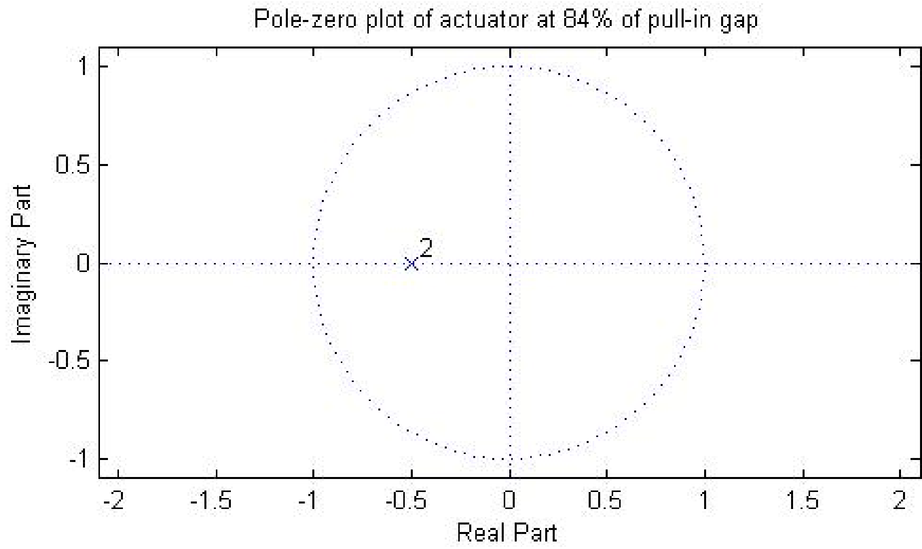

(c) 84% of pull in position

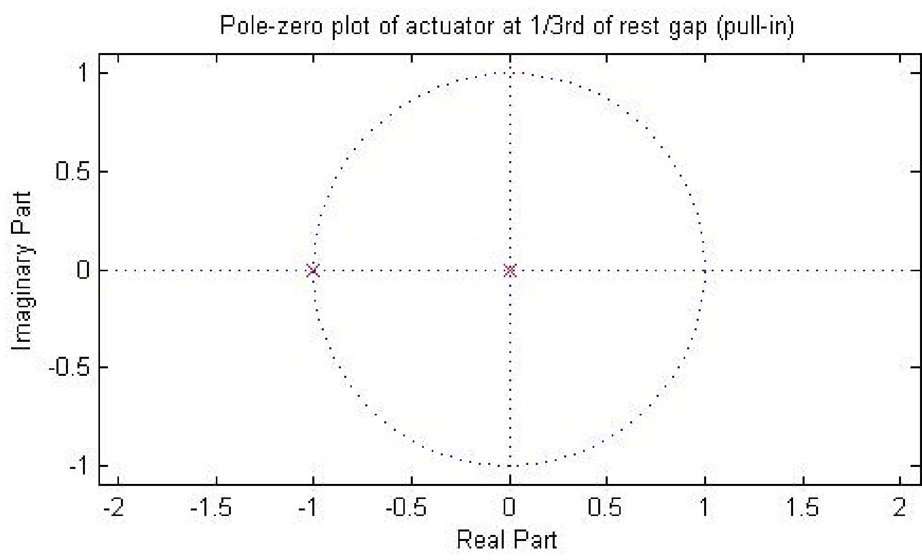

(d) Pull-in Position(1/3 of rest gap)(Unstable)

Figure 2.5: Pole Zero map of actuator at different points of stability

2.2 Motivation

MEMS PPAs have a number of advantages that make them desirable for use in micro systems. However, one issue that must be accounted for is the pull-in instability inherent in them. Depending on its use, the effect of a device entering pull-in can either enhance or be

a detriment to operation. A number of issues can arise when the pull-in condition is reached that can affect the operation of MEMS devices. These issues can range in effect from small signal instability to complete destruction of the device. In these instances, detecting and preventing or mitigating the pull-in event is important to ensure correct operation of the device. The following sections list the potential undesirable effects as well as some benefits associated with pull-in.

2.2.1 Disadvantages of Pull-In

1. Stiction:

   In devices with a large mass, inertial forces are the predominant force explained by the equation $F = ma$, but as the device scales down in size, the mass reduces by the cube of the length. Also as devices shrink, magnetic forces are significantly decreased. Other forces, however, become very important at small sizes. Two of these forces include Van der Waals forces and capillary forces. Van der Waals forces are relatively weak forces caused by charge imbalances between many molecules. When two surfaces come into contact with each other, and these Van der Waals forces are stronger than the restoring spring force of the structures, then the structures will become stuck together. Capillary forces are characterized by the tendency of a liquid to be pulled into a small opening. This movement is caused by attractive forces between the liquid and the material of the wall. At large sizes, the inertial force due to mass would overcome these small forces. But for MEMS devices these forces overcome the inertial forces, causing the device to become stuck. This phenomena is called stiction which is a major cause of yield failure during fabrication, but can also have effects during device operation if two micro-surfaces come into contact, which can happen as a result of pull-in.

2. Current Arcing through Electrode Contact:

   In addition to stiction, the moving plates in MEMS devices can also become fused together through current arcing caused by the large current density forced through a

small area when the plates make contact. This high current can cause the two surfaces to permanently weld together or even vaporize. This will cause catastrophic failure of the device.

3. Damaged Electronics:

   MEMS devices often require high voltages to change plate position. This is especially the case when pull-in is reached. When the two plates come together, the resistance of the circuit can instantly go from very high to very low allowing large current flow. This current can be high enough to exceed the maximum current limits of the electronic circuitry connected to the MEMS device. If the high current flow is sustained long enough, the circuitry can fail permanently.

4. Mechanical Failure:

   Due to the large amount of force generated by the electrostatic voltage between the two plates, mechanical structures in the device can be stressed beyond their fracture limit. This will cause permanent damage to the device.

5. Erroneous sensor readings:

   Many MEMS devices rely on either capacitive or resistive sensing of plate motion to measure signals from the device. Motion of the device is normally limited to very small displacement in order to keep the signal variation as linear as possible. Outside of a small displacement, the signal can become nonlinear and distort the sensor reading. The pull-in event is characterized by large displacement and nonlinear motion which can be deleterious to a system that relies on stable linear motion.

6. Controls techniques to extend the stable range of motion are complex/costly.

2.2.2 Advantages of Pull-in

While pull-in is normally considered an undesirable condition, the phenomenon can also be used to create sensors that respond mechanically to an input stimulus, and create

actuators that can generate a large amount of force. In these instances, it can be useful to detect the occurrence of the pull-in event without inhibiting the effect of the pull-in process. The highly nonlinear motion of pull-in provides opportunities in which the onset of the condition can be detected.

Much research has gone into preventing pull-in by extending the stable range of the actuator. Many of the methods developed to extend the stability range, however, introduce other problems that also must be taken into account such as decreased sensitivity of the actuator, and increased cost of the controlling circuit. Sometimes the pull-in characteristic of PPA's is desired for correct operation. In some cases, actuators do not require the ability of full range of motion, but only to ensure that pull-in does not occur. Also there are times when pull-in is necessary for operation of the device. In these cases, it would be beneficial to detect the onset of the pull-in condition at which point the device can either be shut down when pull-in is unwanted, or when wanted, to keep track of the conditions that caused pull-in to take place. A sensing mechanism can potentially be much simpler and less expensive to implement than existing control systems while at the same time reducing the negative effects associated with other control mechanisms.

2.3 Chapter Summary

In this chapter a detailed derivation of the mathematics describing the motion of PPA's was covered, including the equations governing the force due to a static electric field and motion that occurs during pull-in. The advantages and disadvantages were explained as they relate to various device applications and are summarized below.

- Advantages
    1. Applications that require a device to make mechanical electrical contact.
    2. High acceleration of electrode generates high momentum for actuating objects.
- Disadvantages

1. Damage caused by stiction after pull-in occurs.
2. Current arcing caused by electrical contact of plates
3. Damaged electronics due to high voltage passing through shorted electrodes
4. Mechanical failure of the PPA caused by the excessive force of the pull-in event.
5. Erronius sensor readings from device operating outside of the linear operational range.
6. Increased cost of extra electronics required to overcome the pull-in phenomena.

These examples provide the motivation for the research behind this work to provide a low cost method of identifying when pull-in is about to occur and providing a way of preventing the event or just signaling that it has occurred.

Chapter 3

Literature Review

An exhaustive review of prior work in the area of pull-in as well as various current sensing methodologies has been performed. A summary of key areas of focus in regard to pull-in follows. A number of models describing pull-in from different perspectives have been developed, including frequency considerations [9] and two dimensional modeling to account for off-axis tip-in instability [10]. These areas include device design methods intended to reduce the effect of pull-in, as well as open and closed loop control methods to extend the stable range before pull-in occurs. The following sections provide a summary of the previous work used to control and prevent pull-in.

3.1 MEMS Devices that Make Use of Pull-in

While most MEMS devices attempt to avoid pull-in instability, some devices actually rely on it for operation. Listed below are two examples where this is the case.

1. MEMS Switches:

   The MEMS switch has gained popularity for its fast switching times and very high change in impedance between the on and off states. [11] [12] [13] [14]

2. Gas Flow Actuator:

   A novel structure was Xie et al which uses the pull-in phenomena to create a peristaltic micro-pump. A system of three membrane-based PPA's is made from layers of paralyene to maintain electrostatic isolation with the pumping fluid. The membranes are aligned in a channel and alternate between a closed and open state forcing liquid to move between actuators with each cycle. The frequency of the state changes controls

the speed at which the liquid will flow. With this pump, they were able to achieve a 1.7nL flow rate with a pumping pressure of 1.6kPa [15].

3.2 Actuator Control

1. Open Loop Control

   - Series Capacitor Method:

     In a paper by Seeger et. al, the authors show that the stable range of a PPA can be extended with the simple addition of a series capacitance creating a capacitor divider with the PPA. As the distance between the plates of the PPA decreases, the capacitance relative to the fixed capacitor increases causing a negative feedback where a higher percentage of the total voltage drop occurs across the fixed capacitor. The voltage across the PPA will decrease allowing it to remain in a stable state as the plates move closer together. This technique will allow full range of motion for the actuator provided the correct ratio of fixed capacitor to actuator capacitance is chosen. This method, however, also has drawbacks in that the voltage required to move the actuator is much higher with the fixed capacitor due to the large voltage drop across it. Also, because the voltage can be quite high, the type capacitor required to act as the fixed capacitor in the circuit can be quite bulky due to the required high voltage rating [16]. Additionally, this technique is very sensitive to stray capacitance in parallel with the capacitor. Other groups have since furthered the research into this method by applying it toward different applications. XingTao Wu et. al used the method to model an electrostatic micromirror with increased travel range using this method. [17]

     Another work also used the series capacitor method but then extended the method by closing the loop. They measured the voltage change at the actuator and then applying a current drive to fix the plate at a certain position. They were

also able to reduce the voltage penalty of the series capacitor method using this approach. [18]

- Fabrication Techniques:

  Researcher have investigated creating novel actuator designs to mitigate pull-in. One notable work is by Legtenberg et al. to create a cantilever spring structure with tapered actuating electrodes positioned on the side of the beam which provide both a vertical and lateral force on the beam. As the cantilever moves closer to pull-in, the vertical component of the force reduces due to the positioning and shape of the electrodes. This allows the beam to achieve full scale motion without succumbing to pull-in. While this cantilever spring structure has a much different mechanical operation than that of a PPA, the mitigation of pull-in due to electrode positioning is novel. [19]. Zhe et. al followed a similar method in which they modeled the pull-in effect on various different shapes of electrodes, and found that electrode with certain shapes could achieve much higher pull-in range up to 100% of the gap distance using a power function design. [20].

- Negative Capacitance/MOS Capacitance:

  Variations on the series capacitor method have also been shown to extend the stable range while helping to offset the higher voltage requirement of the fixed series capacitor. By adding a MOS capacitor in depletion as the fixed capacitor, the same negative feedback can be created where the voltage across the MOS capacitor increases as the PPA gap decreases. This voltage increase across the MOS capacitor causes the depletion region to increase reducing the capacitance of the MOS capacitor as the capacitance of the PPA increases. This amplifies the negative feedback of the voltage across the PPA. [21]

2. Closed Loop Servo Control:

   Closed loop Control systems have the ability to extend the range of motion beyond pull-in by providing a feedback mechanism from some monitoring sensor, usually a

sensing capacitor, to a controller which reacts to changes in the monitoring sensor. the controller will change the amount of voltage on the plate as needed to maintain a particular position. This can be done faster than the ability of the actuator to react and is an effective way to control position past the pull-in point. A disadvantage of this, however, is due to the large amount of electronics involved in maintaining the feedback loop. The electronics involved can consist of an amplifier, a lowpass filter, a demodulator, and the controller circuitry. Control of up to 60 percent of the gap distance has been observed, which is well above the one-third pull-in limit. [22]

- Stiffness Control:

  Another idea, presented in a paper by by Hung and Senturia, is to use the notion of leveraged bending to control the position of the actuator. Leveraged bending is the idea of moving a structure by applying force only to a portion of the structure. By positioning the electrodes only at the spring edges and not at the center of the mass, the springs will deflect, causing the mass to move down. As more voltage is applied, the mass will move the full gap distance, while the part being actuated, the spring, has yet to move the one-third gap distance. This idea is similar to the work by Legtenberg for pull-in control on a cantilever, but can also be applied to the PPA. [23]

- Synthetic Voltage Division:

  A work by Dean et al at Auburn University extends the idea of using the series capacitor to increase the stable range by including a feedback controller to reduce required input voltage, which is the main disadvantage of the series capacitor method. [24]

- On-Off Control:

  In a work by Mol et al, a method of digital on-off input is proposed to control the position of the actuator. A feedback controller is created by measuring change in the capacitance of the device, if the capacitance changes past a certain reference

point then the input voltage is shut down. Once the spring reacts and begins to pull back, the voltage is turned on again. The plate remains unstable with respect to the input voltage, but because the switching mechanism occurs at a much higher frequency than the actuator has time to respond, the plate does not snap in. Any gap position can be maintained using this method; however, the device will not come to rest in the unstable region. It will instead oscillate around the control position. The oscillations can be reduced by lowering the voltage level once oscillation begins, and increasing the switching frequency, but complete elimination will not occur. [25]

3.3 Chapter Summary

Most research in the MEMS area on pull-in is devoted to extending the stable range or eliminating pull-in altogether. Most of the solutions that have been discovered either add a great deal of complexity to the circuit or change or influence the operation of the circuit such as causing increased operating voltage. For some purposes, the actuator does not need this level of control, but instead only needs to detect when the event occurs and possibly then to disable the actuator. This can be accomplished using much less circuitry while reducing the impact on the signals controlling the actuator. This dissertation will attempt to examine the various methods discussed earlier and use them to detect the onset of pull-in of a fabricated test device and to disable the actuator power supply before the electrodes make contact.

Chapter 4

Theory Development of Pull-In Sensing Mechanism

In choosing an appropriate method for detecting pull-in in a MEMS device, a number of different options were considered. Many well established sensing methods have been developed, each with their own advantages and disadvantages. Considerations such as sensitivity of the signal, resolution, and size and cost of the sensing equipment must all be taken into account. The following sections will explore the various methods evaluated and the reasons for and against applying each method for this particular application.

4.1 Current Sensing

Current sensing techniques are a well-established area in power electronics and other areas where sensing of high currents is necessary. With enough sensitivity and amplification, these techniques can also be applied to characterize the dynamics of pull-in, and to identify the moment that pull-in occurs. In dealing with smaller currents, one of the best approaches available is resistive sensing, in which a resistor is placed in the path of the current flow, and the voltage drop across the resistor is measured. There are two main techniques that are used when implementing resistive sensing, called high side sensing and low side sensing. These techniques will be discussed in the following section.

4.1.1 High Side Current Sensing

A high side sense circuit is created by placing the resistor between the voltage source and the load as shown in Figure 4.1. At the onset of pull-in, the motion of the movable electrode begins to increase in speed, moving toward the fixed electrode. This movement causes a decrease in gap separation which results in an increase in capacitance in the actuator.

This quick increase in capacitance causes an inrush of current into the actuator to fill up the extra charge storing capability. The result of this current flowing across the high side resistor causes a voltage drop that can be measured and is related to the amount of current flowing into the actuator. Ideally, the resistor has a low impedance in relation to the load so that the current through the loop is not disturbed. The change in voltage is linearly proportional to the change in current across the resistor, assuming an ideal resistor. The resistor then acts as a constant of proportionality where increasing the value of resistance will increase the resulting voltage change for a given current. Additional drawbacks to high side detection are in the measurement method. Normally, the inputs of an instrumentation amplifier are placed at each side of the resistor to amplify the voltage difference. By doing this, the inputs have no fixed reference, but are instead referenced to each other. The amplifier must have a high common mode rejection ratio (CMRR) to reduce any error at the output. [26] Another issue that arises for sensing of this type which can be especially relevant when applying to a MEMS device is that most op amps have a maximum input rating of around ten to twenty volts. The actuation voltage for parallel plate actuators can sometimes reach 50-100 volts, which can easily be high enough to damage the op-amp. A compensation circuit is proposed to solve this problem, which is shown in Figure 4.2. This circuit places voltage dividers with precisely matched resistors on each side of the current sense resistor to create a new sense node with a potential that is reduced from the voltage across the sense resistor by the same ratio as the voltage divider. This allows the sense voltage to remain within the limits of the attached operational amplifier circuit which can act as either a buffer or a gain stage that feeds to a comparator. The comparator then servers as the controller for the detection signal. Once the signal is tripped, the signal trips the clock of a DFF propagating through as an output high on the DFF, remaining so until the circuit is reset. Also included is a protection mechanism, a low R_{ds}-on PMOS transistor is placed in the circuit path which is normally on until the PPA snaps together, at which point the PMOS will turn off effectively breaking the circuit. This is added as a fail-safe to prevent circuit damage, in case the PPA snaps

together. [27] This circuit was tested on a breadboard as a potential solution for detecting and mitigating pull-in. However, while this method still has potential, the initial tests found it to be very susceptible to noise as well as the sensing voltage offset mentioned previously.

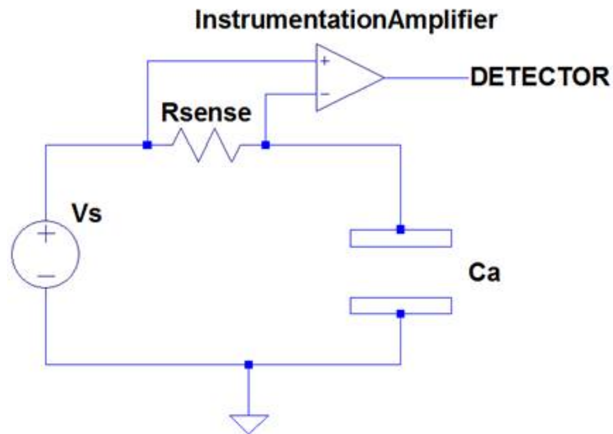

Figure 4.1: Simplified schematic of a high side current sense circuit

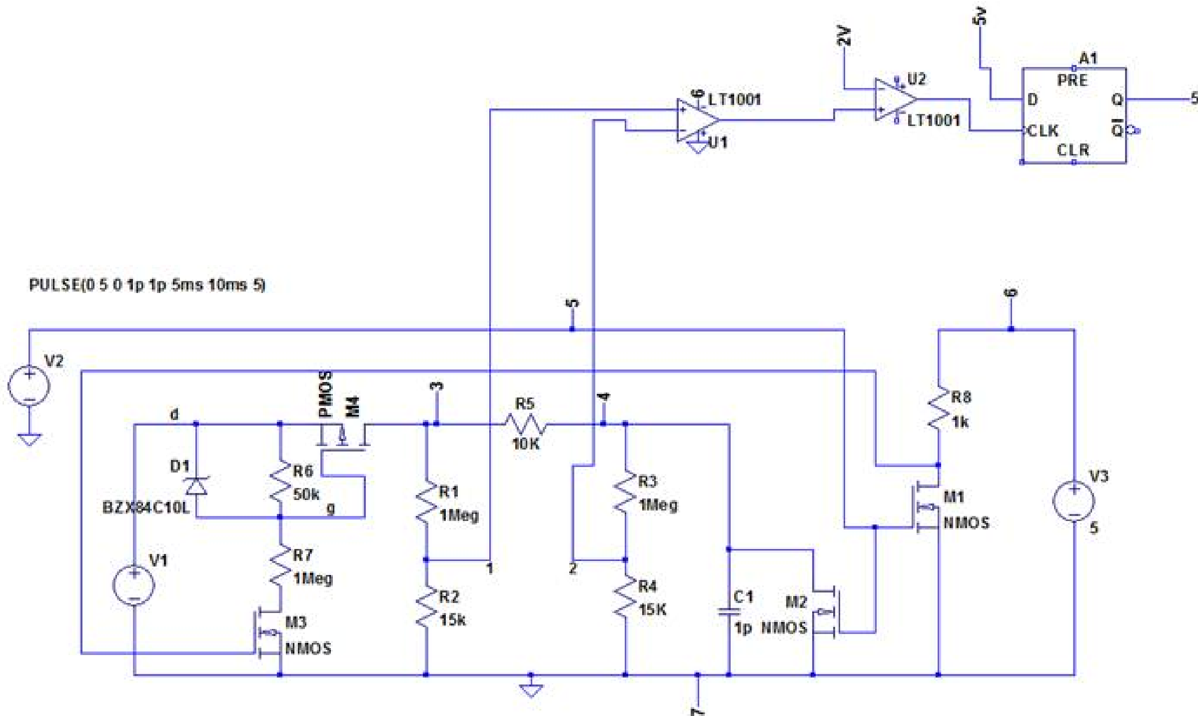

Figure 4.2: Compensation circuit to account for high voltage MEMS devices

4.1.2 Low Side Current Sensing

A low side current sensing is created by placing the sense resistor between the load and ground, and measuring the current across the resistor just as in the high side current sensing method. This is the simpler of the two alternatives because measurement across the current sense resistor has a fixed ground reference. Also there is no need for the high side compensation circuit discussed in the previous section. The disadvantage to this circuit, however, is that the load is no longer attached directly to ground, but rather to a note that has a voltage equal to IR. This can cause problems with some high frequency circuits that require a true ground. [28]

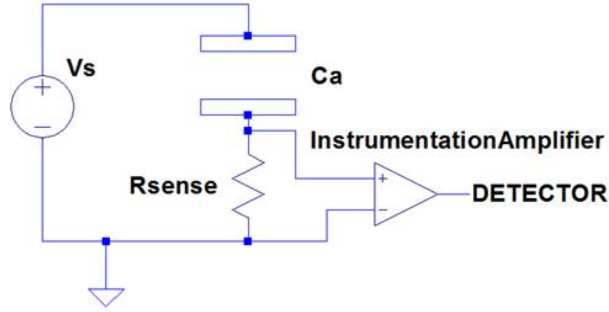

Figure 4.3: Schematic of a low side current sense circuit

4.1.3 Low-Side Transimpedance Amplification Sensing

Low Side transimpedance amplification is an extension of the low-side current sensing method, where instead of measuring the voltage across a resistor, the current is amplified though a feedback resistor connected to an operational amplifier (opamp). A schematic of this method is shown in figure 4.4. The voltage at the output of the opamp is equal to

$$V = -I_{act} R_{Sense} \tag{4.1}$$

Where I_{act} is the current though the actuator, and R_{Sense} is the feedback resistor on the opamp which acts as the gain term for the signal. One side of the actuator is connected to the high voltage source while the other side is connected to the negative input of an opamp. The positive input of the opamp is connected to ground causing the negative input to be taken to a virtual ground. To the actuator, which works at low frequencies, the opamp should be transparent in operation. This method has the potential for very high gain sensing of current into the picoamp levels. [29]

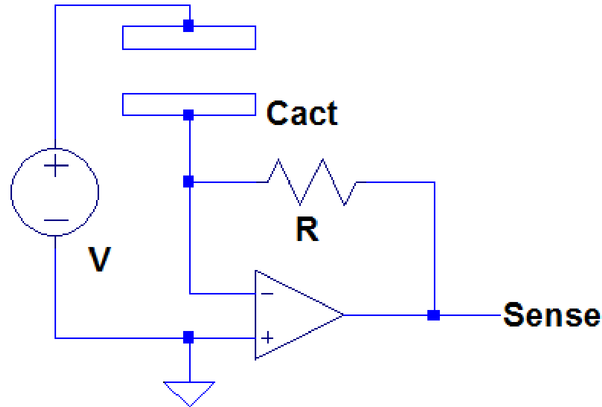

Figure 4.4: Schematic of a transimpedance amplification circuit

4.2 Hall Effect Sensing

Hall effect sensors measure the voltage generated by the force created due to the interaction of a magnetic field on charged particles moving perpendicular to the magnetic field called the Lorentz force shown in equation 4.2.

$$F_{lorentz} = q\left(E + v \times B\right) \tag{4.2}$$

Sensors based on this principle apply a constant current through a Hall element. The current passing through the circuit which is to be measured creates a magnetic field on the current passing through the Hall element. This creates a voltage which is then amplified and measured. The advantage of this technique is that this sensing mechanism is almost completely noninvasive to the circuit allowing current to flow unimpeded, and can sense both ac and dc currents. The potential drawback is that this application is normally used in high current applications to generate the magnetic field required to generate a measurable voltage. It is possible however that if a large enough magnetic field is generated, even smaller currents on the scale that would be required to detect pull-in could be measured. [30]

4.3 Optical Sensing

Another method to detect pull-in is to visually determine that pull-in is occurring using an interferometer. Using a Polytec OFV vibrometer shown in Figure 4.5, the position of the actuator can be converted directly into a voltage that can be measured electrically. The pull-in condition can be detected by the increased slope of the voltage change from the interferometer. This method should have high accuracy with no interference in the operation of the device. The disadvantage of this technique is the large amount of external equipment required to take measurements. [31]

Figure 4.5: Polytech OFV Vibrometer

4.4 Piezoresistive Sensing

Another method of detecting movement of the PPA is by using a piezoresistive element to detect deformation of the spring. A piezoresistive structure changes its electrical resistivity when mechanical strain is applied. This sensing element can be integrated into the actuator springs, and as the spring moves toward pull-in, the resistance will change. This change can be measured using a simple voltage divider or even a Wheatstone bridge. [32] One method of creating a piezoresistive device is to create a diffused resistor on top of the spring by

doping the area. The advantage of this method is that it should have almost no effect on the operation of the device, and external electronic circuitry is very simple. The disadvantages are that this method of sensing is not as linear as other methods to detect motion, and fabrication of the device becomes more complicated to implement because of the extra mask layers required to implement a diffused resistor. [33]

4.5 Secondary Capacitance

Another possible method of detection is to add a separate sense capacitor on the device with a set voltage reference whose sole purpose is for position detection. This would require a change in the design and fabrication of the device, but could be a very accurate method of pull-in detection. This method was successfully used to create a tunable capacitor in a work by Xiao et. al. [34]

4.6 Current Transformer

The current transformer is a well established method of measuring currents in power electronics, particularly in high current applications where it is not feasible to directly measure such a large current. The current transformer consists of a primary and secondary coil where the ratio of the currents between the primary and secondary coil is equal to the turns ratio of the windings in the coils. Because the current transformer operates on the principle of Faraday's law of induction shown in 4.3, it can only measure ac signals. This should be appropriate for measuring the pull-in effect because it is a high frequency signal. [35]

$$\nabla \times E = -\frac{\delta B}{\delta t} \tag{4.3}$$

4.7 Chapter Summary

As this chapter shows, a number of different options exist for sensing plate motion. Each option has its own benefits and drawbacks. There proposed sensing solutions can be categorized into 4 main areas as follows

1. Capacitive
   - Secondary capacitance
2. Current
   - Hall Effect
   - High/low side resistive measurement
   - Current Transformer
   - Transimpedance Amplification
3. Resistive
   - Piezoresistive Measurement
4. Optical
   - interferometric measurement

Because of time and budget constraints, not all of these options could be investigated. Some methods were initially judged to be unsuitable for MEMS application. The Hall effect and transformer applications were judged to have insufficient sensitivity to achieve the stated goal of sensing pull-in. Piezoresistive measurement, while a potentially viable solution, could not be investigated due to the costs required to complete the additional fabrication steps of resistor doping and patterned metal deposition. Optical sensing is very precise, and for this reason it was used as the control for the experiments, but in real world applications, this was not a viable option because large external equipment is required. For these reasons,

current sensing was selected to be the sensing method of choice, specifically, transimpedance amplification due to its ability to achieve very high gain, and little dc offset error.

Chapter 5

PPA Design and Fabrication

This chapter details the processes used to design and fabricate the PPA devices that were in testing. An explanation of the design considerations is given to make the device more suitable to the experiments conducted. These considerations include ease of measurement, maximization of capacitance, and minimization of pull-in voltage. Also covered are the simulations that were used to verify both the design of the device and operation of the detection circuit. Finally, the processes used to fabricate the device are thoroughly discussed.

5.1 Intellisuite Simulation of PPA device

As shown in Figures 5.1(a) and 5.1(b), the actuator structure was designed with long, narrow springs and a large proof mass so that stiction would not be an issue, while at the same time having a low enough pull-in voltage to enable testing with easily accessible equipment. Also, a problem for small silicon actuators is that if the current discharge at snap-in is large enough, the current density through a small surface area can be enough to fuse the surfaces together.

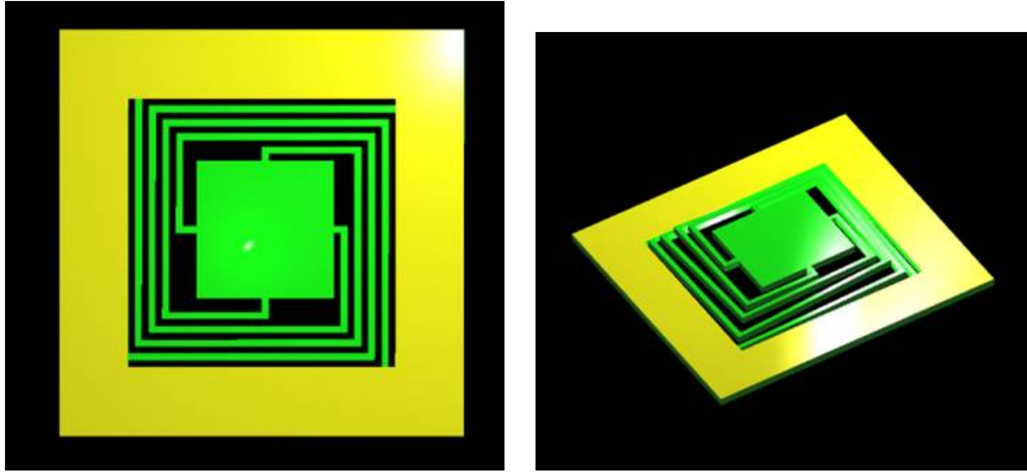

(a) Overhead View (b) Angle View

Figure 5.1: Intellisuite simulation of PPA structure

A Finite Element Analysis (FEA) was performed on a model of the device using Intellisuite, a FEA software tool, to simulate the mechanical response of the device. The table in figure 5.1 shows the simulated resonant frequencies of the first 5 resonant modes. The primary mode natural frequency though simulation was found to be 248 Hz. Once the device was fabricated, the device was placed on a mechanical shaker to determine the transmissibility curve. The resulting curve showed peak transmissibility at 227 Hz, which is relatively close to the simulation prediction. The deviation in frequency was attributed to simulation assumptions, variations in the material properties, and fabrication tolerances.

Mode	Frequency (Hz)
1	248.844
2	463.556
3	464.521
4	523.326
5	523.52

Table 5.1: Intellisuite modal simulation of designed PPA device.

One consequence of designing a device in such a way that the springs wrap around the device, as in this case, is that in deformation, the mass has a tendency to rotate. Since, in this experiment, displacement is limited to 150 μm this rotation effect was considered negligible. Another effect of the extended spring length is that higher order vibration modes have resonant frequencies only slightly higher than the primary mode. This off axis movement could cause an unintended reduction in capacitance, as well as cause an imperfect surface contact between the two electrodes when snap-in occurs causing incomplete charge dissipation. While capacitance variation was not found to be a significant source of error, contact quality had a major effect on oscillation reliability. It was determined that off-axis vibration was not the main contributor to the contact quality issue. Contact cleanliness and non-uniform plating of the PCB electrode also played a significant role.

5.2 Simulink Simulation Pull-in Detection Operation

In order to make the parameters of the simulation as close to as accurate as possible, a fabricated PPA was characterized so the actual parameters of the device could be entered into Simulink. The damping coefficient was found through measuring the transmissibility plot and reading the value at the device's resonant frequency, which was approximately equal to Q. A graph of this, as shown in Figure 5.2, shows the device having a natural frequency of 227Hz with a Q value of 46. [36]

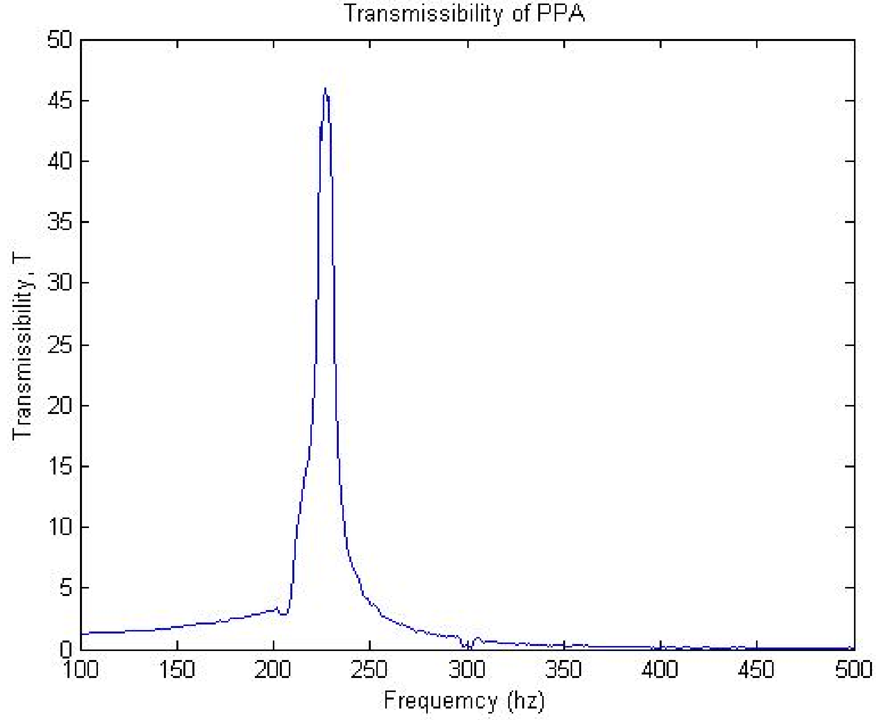

Figure 5.2: Transmissibility of the fabricated PPA

Table 5.2 lists the final properties of the designed PPA which were used to generate models to compare the performance of the device in operation. The spring constant was estimated using equation 5.1

$$k_{eq} = \frac{N_{leg}}{N_{Zig}} \frac{Ewt^3}{L^3} \tag{5.1}$$

where k_{eq} is the equivalent spring constant of the 4 combined springs. N_{leg} is the number of springs attached to the proof mass. N_{Zig} is the number of 90 degree bends in each spring. E is Young's modulus for silicon, w is the width of each silicon spring, t is the thickness of the springs, and L is the total length of each spring. The damping coefficient was then inferred from the experimental Q factor obtained through vibration testing.

PPA Device Properties	
Spring l,w,t	55250μm 50μm 375μm
Actuator Area	0.0001 m^2
Actuator Mass	0.000094125 kg
Spring Constant, k	22.0125 $\frac{N}{m}$
Rest Gap	1.50E-04m
Q-factor	46
Damping coefficient	0.000968477
Rest Capacitance	9.5pF
Natural Frequency	227Hz

Table 5.2: Parallel Plate Actuator Device Properties

A model of the parallel plate actuator was created in Simulink using the equations presented in section 2.1. The parameters for the device were found using standard MEMS equations. A list of the parameters of the device is shown in Table 5.2.

Figure 5.3 shows a diagram of a Simulink program that implements a simple one dimensional mass spring damper system using the values shown in table 5.2. A ramping voltage is converted to an electrostatic force value and applied to the summing node of the transfer function. A saturation value is added with the rest gap value to show the maximum range of travel for the PPA. The values are then fed into a function which calculates the current at any given time through the actuator. This simulation assumes ideal properties, including perfect voltage sources, linear spring constant, negligible resistance, and constant damping. All of these can contribute to variations from the exponential results of the fabricated PPA.

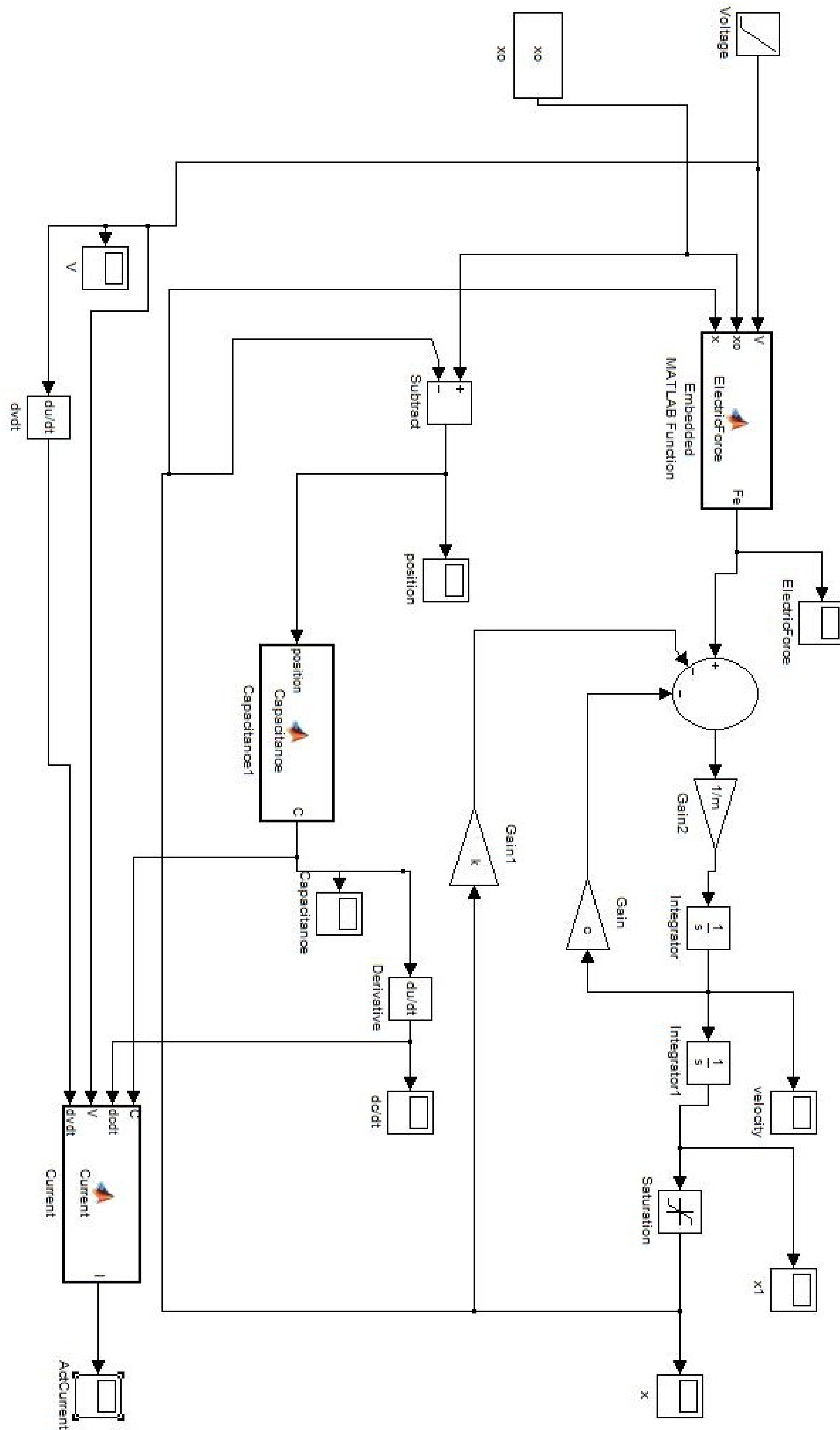

Figure 5.3: Simulink Model of PPA

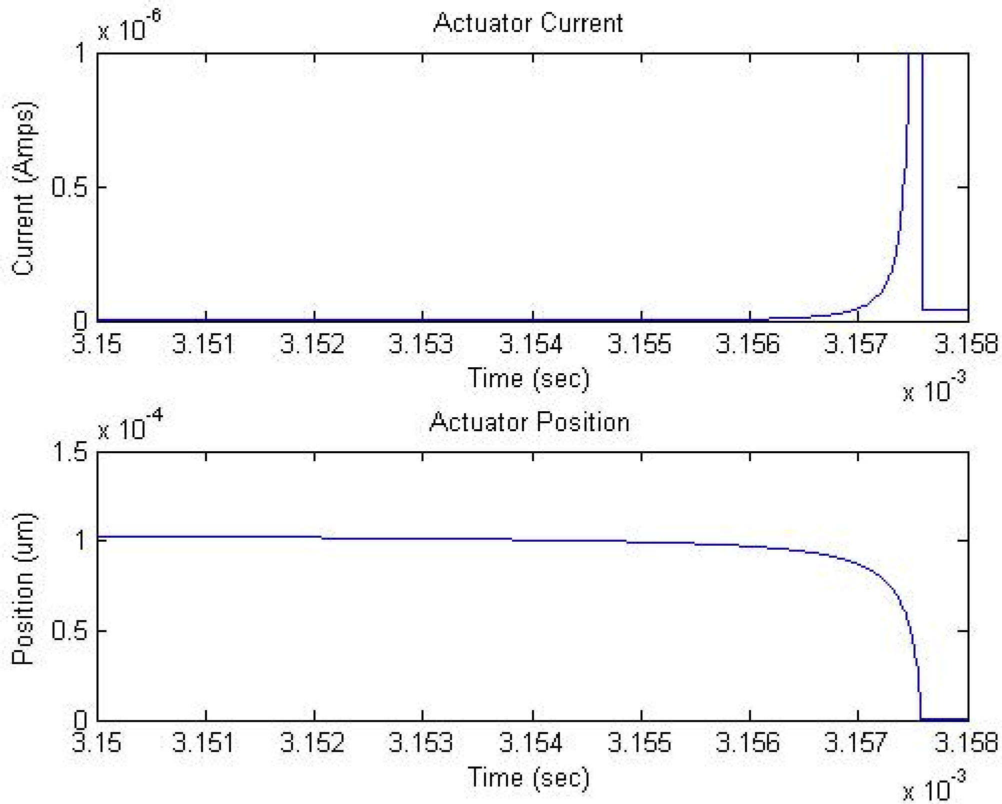

Figure 5.4: Current and Position Results of Simulink PPA Under Ramping Voltage.

The simulation shows as expected that as the voltage across the actuator increases above the pull-in value, the movable plate increases in velocity moving rapidly toward the opposing plate. Also, the current begins to increase exponentially as the velocity increases.

Table 5.3 shows sample current values at different positions after pull-in has begun. At each position, the current increases by an order of magnitude which can be detected very quickly.

Simulink Results	
Position	Current
1.00E-04μm	1.67e-9A
7.00E-05μm	2.5e-7A
5.00E-05μm	1.3e-6A
4.00E-05μm	2.5e-6A
1.00E-05μm	4.85e-5A

Table 5.3: Simulink Analysis of Current as a Function of PPA Position

5.3 Fabrication Equipment and Processing

The Alabama Microelectronics Science and Technology Center located at Auburn University is equipped with all of the tools necessary to facilitate the fabrication of MEMS devices. This equipment, and the parameters by which theory was used, will be referenced heavily throughout this document. In the next few sections, a brief description of the most frequently used pieces of equipment and their operation will be discussed.

5.3.1 Cleaning Equipment and Processes

As explained in various sections of this work, cleanliness plays an important role in the successful fabrication of microelectronic as well as MEMS devices. Wafers undergo thorough cleaning processes between each processing step. The first step in silicon wafer processing is the RCA clean. This step is needed to remove contamination on the silicon wafer that can interfere with future steps in the process.

Before a silicon wafer can be processed, the surface must be clean of particles and impurities which can reduce the quality of the pattern, cause interference in the operation of electrical devices, and become a source of contamination in processing equipment such as the oxidation furnace. To remove these particles, William Kern, in 1965 with the RCA

corporation, developed a cleaning process known as the RCA clean which has since become the standard in the industry. This process involves soaking the wafer in a series of chemical mixtures, each mixture serving a different cleaning purpose. Presented below is a table listing the standard processing steps used in the RCA clean to prepare the wafer for processing. [37]

Table 5.4: RCA Process

Process Name	Step	Mixture	Time	Temperature	Purpose
	A	IPA bath	1Min	Room Temp	Oil Removal
		DI Water Bath	1 Min	Room Temp	
SC-1	B	1 : 30% H_2O_2 1 : 29% NH_4OH 5 : $DI\ H_2O$	5 Min	70°	Removes organic impurities
		DI Water Bath	1 Min	Room Temp	
	C	1 : 49% HF 50 : DIH_2O	30 Sec	Room Temp	Removes Hydrous Oxide
		DI Water Bath	1 Min	Room Temp	
SC-2	D	6 : $DI\ H_2O$ 1 : 30% H_2O_2 1 : 37% HCL	5-10 min	70°	Removes Heavy Metals
		DI Water Bath	1 Min	Room Temp	

Standard Clean 1 (SC-1)

The SC-1 solution is a mixture of 5 parts DI water, 1 part 30% concentration H_2O_2, and 1 part 29% concentration NH_4OH heated to $70°C$. The wafer is submerged in this solution for 10 minutes. During this time, the H_2O_2 creates a hydrous oxide layer on the surface of the wafer, while the NH_4OH acts to remove this layer. This process repeats continuously and results in the removal of organic materials, light metals and other small particles on the surface of the wafer. Once this step is complete, the remaining hydrous oxide layer must then be removed. This is done by dipping the wafer in a mixture of 50 parts DI water, and 1 part HF acid at room temperature for approximately 30 seconds. [38]

Standard Clean 2 (SC-2)

The SC-2 solution is a mixture of 6 parts DI water, 1 part 30% concentration H_2O_2, and 1 part 37% concentration HCL heated to $70°C$. The wafer is submerged in this solution for 10 minutes. This step removes heavier metals that are not removed in the SC-1 step. [38]

Spin Rinse Dryer

The STI Semitool Spin Rinse Dryer shown in Figure 5.5 is a tool designed to assist in maintaining a particle-free wafer.

Figure 5.5: Spin Rinse Dryer

There are two versions available in the lab to accommodate 100mm and 125mm diameter wafers. This device sprays deionized water across the surface of the wafer, while spinning, to remove particles and other loosely held contaminants. The wafer then enters a drying

phase where the spin speed of the wafer is increased, and heated nitrogen is blown across the wafer to remove the water from the previous rinse cycle. This step is important for cleaning wafers during multiple steps of the fabrication process.

5.3.2 Patterning Equipment

After cleaning the wafer, a pattern can then be transferred to the wafer that will realize the intended design. This pattern is normally created using PR. This is a material that is sensitive to light and acts as a masking material to other processes.

Hexamethyldisilazane (HMDS) Chamber

Before PR can be applied to the wafer surface, the wafer must be primed to accept the resist. At room temperature, water molecules from the air can attach to the wafer surface causing PR to attach to the water molecules instead of the silicon. To remove the water, the wafer is placed in a dehydration oven and heated to $120°C$ for twenty minutes. After dehydration, a primer of HMDS is then coated over the wafer which adheres well to both the silicon and the PR.

HMDS is normally applied in one of two ways. One way is to pour the HMDS onto the wafer in liquid form and spin the wafer until only a very thin coating of HMDS remains. The HMDS must then be dried completely before the resist can be applied. This method has the advantage of being easily added to the fabrication process, but has drawbacks in that most of the HMDS is wasted during spinning, and if the HMDS is not completely dry, the HMDS can break down the bottom layer of PR, reducing adhesion instead of improving it. [39]

The second method is to apply the HMDS in vapor form. Because only a few monolayers of HMDS are required to adhere to the resist, the HMDS can be allowed to evaporate and the vapor flows over the wafer. The molecules that attach to the wafer will provide a sufficient amount of coating needed for resist adhesion. This is the method used at Auburn. Shown

in figure 5.6 is the chamber in which the HMDS is allowed to evaporate and attach to the wafer.

Figure 5.6: Vapor HMDS Application Chamber

Photoresist Spinner

A photoresist spinner is used to accurately control the thickness of the PR film applied to the wafer. A uniform thickness is achieved by spinning the wafer at varying speeds and allowing the PR to spread over the entire surface area. Slower rpm's will give a thicker coating, while faster rpm's will give a thinner coat. Longer spin times will help to increase the uniformity of the coating over the wafer.

Figure 5.7: Photoresist Spinner

Matrix Oxygen Plasma Asher

The Matrix oxygen plasma asher is a type of plasma etcher that is used to remove organic material from the surface of the wafer, usually PR. The oxygen plasma reacts with the PR forming an ash that is then removed by a vacuum pump. The parameters that can be modified include the power of the plasma, the flow of oxygen, and the time of exposure. This device has two main roles in MEMS processing. The first is called a descum step. This is a short interval treatment meant to remove excess unwanted PR from the UV exposed areas of a developed pattern. This step is particularly important when the process calls for a wet chemical etch. Even a very thin film of PR that has not been fully removed will completely mask the pattern from etching. The second role this device plays is to fully strip the remaining PR after processing is complete.

Figure 5.8: Matrix Oxygen Plasma Asher

Karl Suss MA/BA6 Contact Mask Aligner

This device creates a pattern on a PR film by bringing a photolithography mask in direct contact with the surface of the wafer and subjecting the exposed areas to a UV light

source. This equipment has the capability of achieving a maximum resolution of 0.7μm, and performing backside alignment functions which are essential for creating the 3D structures involved in this project. A high intensity Hg lamp provides a UV light source for PR exposure, which operates at 365nm (i-line) and 436nm (g-line). Wafer sizes of up to 150mm can be patterned using this equipment. [40]

Figure 5.9: [Karl Suss MA/BA6 Contact Mask Aligner

5.3.3 Silicon Processing Equipment

Silicon is a very strong material with compressive strength up to 80% to that of steel, making this material very useful in MEMS devices. While having a very strong compressive

strength, it lacks the ability to bend plasticity, meaning that the material can fracture easily when bent. Specific tools have been developed that can create structures on the desired scale, while preventing fracture. Using a DRIE system, precise etching can make deep grooves in the silicon, and CVD systems can deposit silicon with very high accuracy. Furthermore, oxidation of the silicon to form silicon dioxide can protect the surface from chemical reactions, as well as forming an electrically insulating barrier.

5.4 Plasma Assisted Dry Etching of Silicon

The aspect ratio of a structure is a measure of the structure's longer dimension compared to its shorter dimension. The aspect ratio for the device being constructed is required to be very high, therefore the structure is fabricated by bulk micromachining a pattern of ridges using an ICP (Inductively Coupled Plasma) DRIE (Deep Reactive Ion Etching) system.

Plasma based etching of silicon has been around for many years, but only within the last twenty years has the technology evolved so that plasma based etching could be utilized for precise directional etching. The following sections will explain how plasmas are used to etch silicon, and discuss some of the modifications that have been made that have allowed for the anisotropic profiles created using the DRIE process.

5.4.1 Plasma Etching

Plasma is an ionized gas that consists of a high density of free electrons. This condition can be created by exposing the gas to a high electric field. As the energy from this electric field is imparted to an atom in the gas, an electron in the outer shell gains enough energy to break free of the atom, thus the atom becomes ionized. Because the electrons are much lighter than the ions, they accelerate much faster in the presence of the electric field. As the electrons move in the electric field toward the electrode, some electrons can become trapped in the chamber wall creating a net negative potential, pushing away other electrons, and attracting ions. This force creates a sheath at the edge of the plasma with a very

high electric potential thus accelerating the ions through the sheath, leaving a nearly charge neutral region at the center of the plasma. The benefit of creating a plasma when used for etching a material is that the energy imparted to the ions can cause reactions with other materials that would normally occur only when they are thermally excited to thousands of degrees K. By creating a plasma consisting of gas compounds that contain either fluorine or chlorine, silicon can be nearly isotropically etched by placing the wafer inside the plasma allowing the excited species to chemically react with the silicon to form new gaseous species such as SiF_x or $SiCl_x$ which are the pumped out of the plasma chamber. This reaction occurs at all points where the etching gas comes into contact with the silicon and is nearly directionless. [41] [42]

5.4.2 Reactive Ion Etching

Reactive Ion Etching is a modification of the plasma-based etching by positioning the silicon wafer at the bottom of the chamber below the generated plasma. This allows etching to occur through the physical bombardment of the energetic ions exiting the sheath of the plasma. In this method, physical sputtering and chemical reaction both occur to enhance the silicon etch. Noble gases such as argon can cause physical bombardment that can break off silicon atoms and give a directionality to the etch that is perpendicular to the surface, while remaining unreactive with the surface. Ions such as fluorine and chlorine also impact the surface and contribute to sputtering, but upon impact they form a chemical reaction with the silicon converting it to a gas such as SiF_4. Other gasses like oxygen, when added to the plasma, have an opposing effect when reacting with the surface forming a passivating SiO_xF_y layer. The SF_x ions also work to remove this passivisation layer. The alternating generation and removal of this layer also helps to change the profile of the etch. Therefore, the SF_6 to oxygen ratio is very important in controlling the anisotropic nature of the etch. [43]

5.4.3 Inductive Coupling of Plasma

A further modification of the plasma generation method is to use an inductive element that is tuned to the frequency of an RF power source. A large amount of current will flow through this inductive element, causing a varying magnetic field inside of the plasma. This changing magnetic field will cause an RF electric field in the plasma which accelerates the ions through the sheath. Generation using this approach can create higher plasma densities which increase both the directionality and the rate at which the silicon is etched. [44]

5.4.4 Deep Reactive Ion Etching

Finally, one last improvement in the plasma etching process, referred to as the Bosch Process, because it was developed by Laermer and Schilp of Bosch, was to combine separate etching and passivating cycles to the Reactive Ion Etching process. [45] This is the process used at Auburn for anisotropic silicon etching. First, the standard cycle using SF_6 and O_2 plasma etches a trench in the surface of the silicon. Then a second cycle of C_4F_8 plasma reacts with the SF_6 to create a Teflon® like coating that covers the bottom and sides of the trench to prevent further etching. The etching cycle is then repeated and the SF_6 and O_2 ions bombard the surface dissolving the passivisation layer at the bottom of the trench and etching further into the silicon. Because the ions arrive mostly perpendicular to the surface, they do not dissolve the passivisation layer on the sidewalls thereby leaving the silicon to the side untouched. Very high aspect ratio trenches can be achieved using this process with reports as high as 107. [46]

The STS Advanced Silicon Etcher (ASE), shown in figure 5.10, uses all the methods mentioned previously to perform DRIE on silicon to create a very high aspect ratio etch. An inductively coupled plasma etches the silicon surface using chemically reactive SF_6 ions. Using an induction coil to generate the plasma has the benefit of being able to create a very high density plasma, and because the coils are located outside of the chamber, contamination that is associated with other methods of plasma generation does not occur. The platen, onto

which the wafer is attached for etching, is connected to a RF source that has two settings at either 13.56MHz or 380KHz. A Bosch process is implemented to create an anisotropic etching profile by subjecting the surface to multiple SF_6/O_2 etch and C_4F_8 steps. [45]

Figure 5.10: STS Advanced Silicon Etcher

Multiple parameters can be altered which modify the etch profile. These parameters include the following:

- Gas Flow Rate

  The mixture of O_2 to SF_6 determines how aggressively silicon is etched. The higher the ratio of SF_6, the faster and more isotropic etch is during each cycle.

- RF Power

The power of the plasma determines the amount of directionality the ions have toward the wafer surface. An increase in the power will cause a more anisotropically etched structure.

- Frequency

  There are two frequency settings available for use. The first is 13.6 MHz and the second is 380 KHz. Use of the 380 KHz setting can cause a phenomenon known as footing at the interface between the Si and the SiO_2 etch stop layer in which energetic ions can become trapped in the SiO_2 layer giving it a positive charge. This charge deflects incoming ions as it approaches the surface, causing the etching species to etch the sidewalls at a higher rate. A common issue associated with DRIE etchers that can increase the likelihood of footing is an occurrence known as the bulls-eye effect. This effect is characterized by the non uniform etching of silicon across the surface of the wafer. The silicon has a tendency to etch at a faster rate toward the edge of the wafer than in the center. In order to completely expose the SiO_2 layer over the entire wafer, some portions will be required to be over etched. This over exposure of the oxide layer to ion bombardment increases the likelihood of footing. By using the low frequency setting, the surface can be over etched without resulting in the footing effect. [47]

- Etch cycle time verses passivisation cycle time

  The ratio of etching to passivisation plays a role in the aspect ratio of the structures. An increase in the etching ratio will allow more silicon etching during each cycle and increase the amount of lateral silicon etching under the pattern. An increase in the passivisation ratio will increase the time required for the etching gas to break through the passivisation layer, thus shortening the amount of time silicon is exposed for etching.

A number of different research groups have used the preceding variables to control the sidewall profile effectively. One group used an alternating sequence of the Bosch process with an isotropic dry etch to create tapered sidewalls with a precisely controlled angle. [48]

Another group created very high aspect ratio trenches by slowly increasing the flow of SF_6 during processing. This increase compensates for the reduced ability of the ions to reach the surface at deeper trench depths maintaining a consistently high aspect ratio. [49]

The etch recipe called MORGNSOI was used for etching all of the silicon wafers in this project. The parameters of this process are shown in Table 5.5.

Table 5.5: MORGNSOI DRIE Recipe

Cycles				
	O_2	SF_6	C_4F_8	Time
Etch Cycle	13 sccm	130 sccm	0 sccm	13Sec
Passivate Cycle	0 sccm	0 sccm	85 sccm	7 Sec
Power				
	Range	tolerance	match load	match tune
13.6MHz connected to Coil	600W	99%	50%	50%
Platen connected to 13.56mHz	0-300W	99%	50%	50%
Helium Leakup				
Test Time	30 Sec			
Max Leakup Rate	30mTorr/min			

Oxidation Furnace

The oxidation furnace, used to oxidize silicon, is a three tube horizontal furnace that uses a controlled flow of oxygen, hydrogen, and nitrogen gas to control oxide growth. Pure oxygen can be used to grow extremely pure thin layers of “dry oxide”, while the addition of hydrogen allows for thicker but lower quality “wet oxide”layers. Nitrogen is also used to both prevent oxide formation, and to purge the chamber of impurities. The furnace is a three zone resistance heated furnace that can be set to temperatures between 400 and 1200 $^{\circ}C$.

Figure 5.11: Oxidation Furnace

5.4.5 Electron Beam Evaporation and Sputtering System

The CHA Mark 50 electron beam chamber shown in Figure 5.12 is used to deposit metal layers on the surface of a device with high accuracy. The system dposits material by using a magnet to focus the electron beam onto a target crucible of the metal. The metal then evaporates and is deposited onto wafers suspended in a planetary above the crucible. This process takes place under a high vacuum which results in a very high quality film that can be deposited at a high rate (50-500nm/min). [50]

Figure 5.12: CHA Mark 50 dual E-beam/sputter/ion gun deposition system

5.4.6 Masking Materials

When creating the masking layer for a macro-scale MEMS pattern that will undergo plasma etching, a high selectivity between the masking material and silicon is desirable. If the selectivity is low, a thicker mask is required to withstand the hundreds of cycles of etching to which it is exposed. The selectivity of materials can vary with changes in the density, power, etching time, frequency, and chemical composition of the plasma. Changes in any of these variables to increase selectivity, however, can also have negative effects on the silicon etch rate, the amount of undercut, as well as the roughness of the sidewalls.

SiO_2 can be effectively used as an etching mask and has high selectivity at about 100-1. Unfortunately, the time required to grow oxide increases exponentially with thickness, therefore, growing enough oxide to withstand etching through a full wafer is not feasible.

For very deep structures, thick film photoresists can be used to mask the etching process. Photoresist can have selectivities comparable to SiO_2, but can be applied in much thicker films. If the film thickness requirement becomes too high, the pattern resolution can be affected. Photolithography equipment can resolve patterns to a very small resolution. Associated with any particular resolution, there is a certain vertical tolerance called depth of focus, within which the pattern will remain in focus. Depth of focus can be defined by equation 5.2

$$DOF = \frac{k_2 R^2}{k_1^2 NA} \tag{5.2}$$

Where k_1 and k_2 are process dependent constants, NA is the numerical aperture, and R is the resolution to be achieved. In order to resolve a smaller feature, the depth of focus must be lowered. If the masking photoresist is too thick, the pattern will not maintain focus through to the surface of the resist, causing some areas to remain unexposed. [50]

5.4.7 Silicon Oxidation

It is well known that oxygen reacts with crystalline silicon to form SiO_2. This property is one of the major reasons silicon has found such widespread use in the electronics industry. The high insulation value of SiO_2, and the ability to precisely control the thickness of oxide that is formed make it ideal for electronics devices such as MOS transistors and capacitors. Another property of silicon dioxide is that it is a very stable molecule both thermally and chemically, making this material useful for protecting the silicon during processing, and chemical etch mask.

5.5 Chapter Summary

This chapter provides a detailed analysis all of the steps involved in the design and fabrication of both the PPA test device and the detection and controlling circuit in which the device will be used. An FEA analysis of the PPA device was performed to verify the mechanical properties of the final device. From there a simulation of the mechanical and electrical operation of the device was performed in Simulink to verify the design works as expected. The fabrication tools and processes were then detailed to give an understanding of how the device was created. The entire final fabrication process can be found in Appendix A.

Chapter 6

Experimental Verification of Pull-in Detection and Mitigation

A test structure was fabricated to verify the simulations from the previous section. The actuator created was a silicon structure fabricated using typical MEMS fabrication techniques of photolithography and Deep Reactive Ion Etching (DRIE) on a $375\mu m$ thick p100 silicon wafer with $0.1\Omega - cm$ resistivity. The photolithography mask was created using a program called ViewMate.

The entire PPA fabrication process is relatively simple with only a few steps. First, the wafer is cleaned using the RCA clean detailed in table 5.4. The wafer is then patterned by exposing and developing a layer of photoresist using the photolithography mask. The wafer is placed on a backing wafer using a temporary bonding material maintain mechanical strength during the etching process. A thin layer of photoresist often works well as a thermally conductive bonding material. The exposed areas of the pattern are etched all the way through the silicon wafer using a DRIE process, specifically the MORGNSOI program listed in table 5.5. Once etching is complete the Individual devices are removed from the backing wafer and gently cleaned in a bath of acetone followed by a weak phirana etch solution consisting of 4 parts H_2SO_4, 1 part H_2O_2. These two processes should clean all of the photoresist and passivisation residue left on the surface of the parts. Finally, the devices are mounted on a holding wafer and suspended in an e-beam deposition chamber to deposit a solderable metal contact of titanium and copper. The complete description of the metal deposition parameters are listed in Appendix B. The full traveler for this process is shown in Appendix A

The MEMS device was suspended over an electrode printed on a PCB, shown in Figure 6.3, by a non-conductive spacer of a set $150\mu m$ width, allowing the MEMS movable plate to

move up and down relative to the fixed plate on the PCB. When operating with resistances greater than $1M\Omega$, performing accurate measurements on electrical characteristics can become problematic because the input resistance of many measurement tools is less than the resistance of the system. For this reason, measurement of the displacement of the actuator was performed using an interferometer which affords a non-electrical measurement of the system dynamics.

6.1 Schematic and Layout of Test Platform

To test the device, a transimpedance amplification circuit was designed in LTSpice. The circuit consists of a transimpedance amplifier connected to a comparator which compares to a reference voltage set to the value at which pull-in occurs. When the current reaches a large enough pull-in value, the comparator goes high initiating the clock input of a positive edge triggered flip flop. The flip flop then initiates the shut-down mechanism of the circuit. In order to safely cut the voltage from the actuator, two operations must be performed. First, the actuator electrodes need to be brought to the same potential. This is achieved by connecting the drain and source of an N-channel MOSFET with a low Rds-on resistance, and a high maximum Vds breakdown voltage, between the high side PPA electrode and ground. The charge can then quickly flow from the actuator to ground reducing the force on the actuator. Second, the voltage supply must be disconnected from the circuit, preventing the newly shorted actuator from pulling a constant current from the voltage source which could damage the voltage source if the series resistance is low. Isolation of the voltage source is achieved by using a P-channel MOSFET with a low Rds-on resistance and high Vds breakdown voltage. The gate of the Pmos is connected to a resistor divider in series with an nmos transistor. Before pull-in occurs, the nmos transistor is active causing a voltage drop across the resistor divider providing the voltage necessary to turn the transistor on. Because the source voltage of the resistor divider is variable, a zener diode is included to ensure that the voltage on the pmos gate does not go above the maximum rated value. A drawback to

the resistor divider configuration, however, is that below a certain value of source voltage, the drop across the resistor may not be enough to fully turn on the PMOS. This low voltage value can be tailored by the value of the resistors used. Figure 6.1 shows the entire electrical schematic implementing all of the previously mentioned functions.

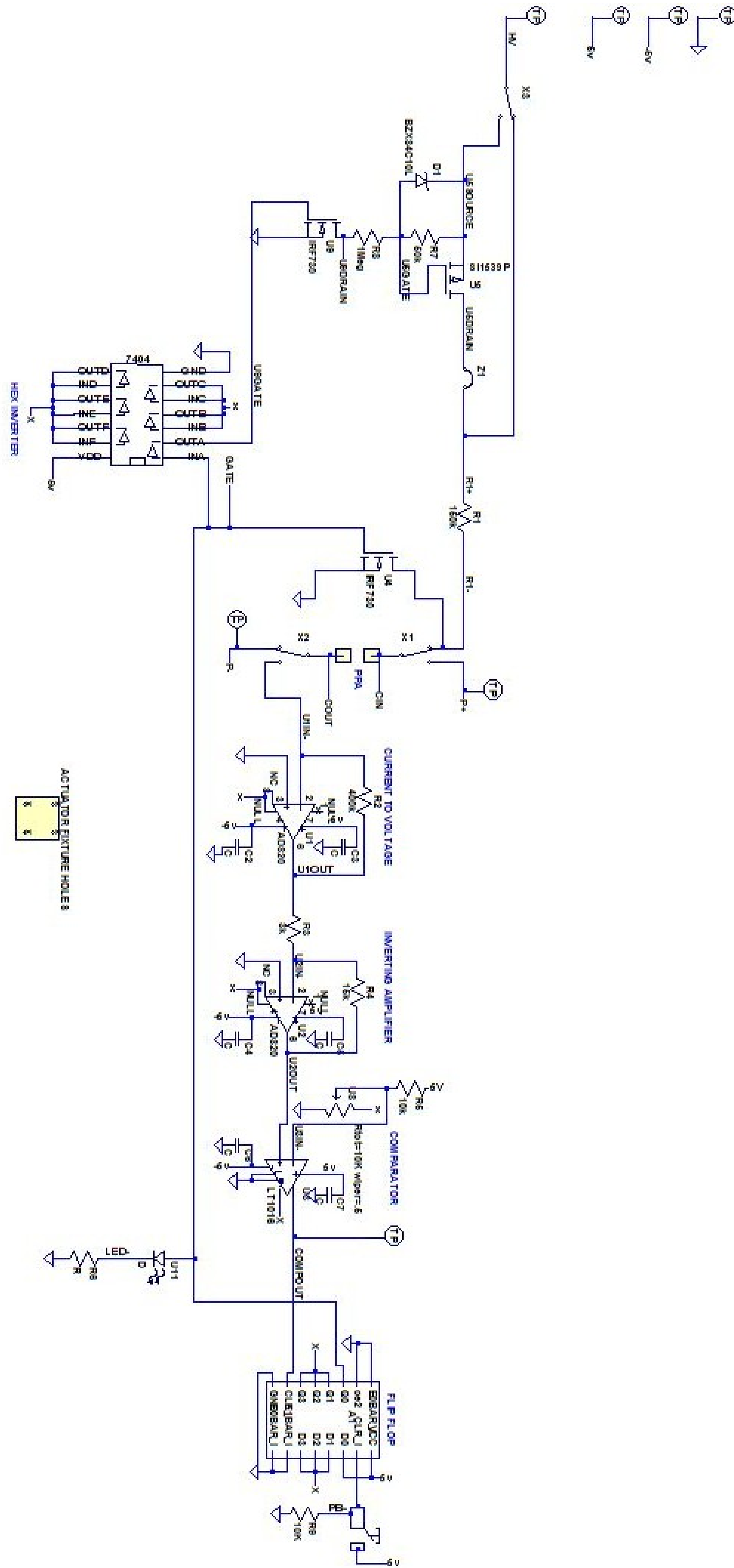

Figure 6.1: Electrical Schematic of Transimpedance amplifier Pull-in Detection Circuit

Figure 6.2 shows the PCB layout of the schematic from Figure 6.1. This layout was completed in a program called FREEPCB. The green areas represent copper on the top of the board, while the red areas represent copper on the bottom of the board. The gray areas are drill holes for vias, through hole parts, and board mount locations. The blue areas represent silk screen on the top of the PCB, and the yellow areas represent silk screen on the bottom of the PCB. The PPA is mounted over the two square pads in the center of the board. The outer square pad acts as a fixed distance mount so that the entire device is equal in height above the center contact. The inner square pad is the bottom fixed electrode. The headers x1 and x2 were placed to allow for disconnection of the entire detection circuit from the PPA device to connect to an external circuit for future testing. Both safety mechanisms are located at the left side of the circuit board as shown by the three through-hole power mosfets. The three 8-pin dip packages are the transimpedance amplifier, a small gain stage, and a comparator. The opamps used are TI TLE2071 high speed low noise jfet input opamps, and the comparator is a linear technologies lt1016 ultra fast precision 10ns comparator. The output of the comparator feeds to a 74hc374 positive edge triggered flip flop, the output of which feeds to both an led with a reset switch to show that the circuit has been tripped, as well as an 74hc04 inverter which provides the correct signal to shut down the safety mechanism.

As information, the following is a list of observances that may be helpful in future work.

- Because such a large amount of gain is required in the amplifiers, the circuit became very susceptible to noise. Large instantaneous changes in the DC power supply would cause enough noise to trip the circuit. Also, physical disturbances large enough to displace the PPA electrode would also sometimes be enough to trip the circuit.

- Traces had to be shortened to as short a length as possible because external interference would be picked up on long wire runs.

- Precise tightening of the compression fixture was required to alleviate stress on the springs which could cause the plate to tilt.
- More test points were needed at critical points in the circuit to make testing go more smoothly.

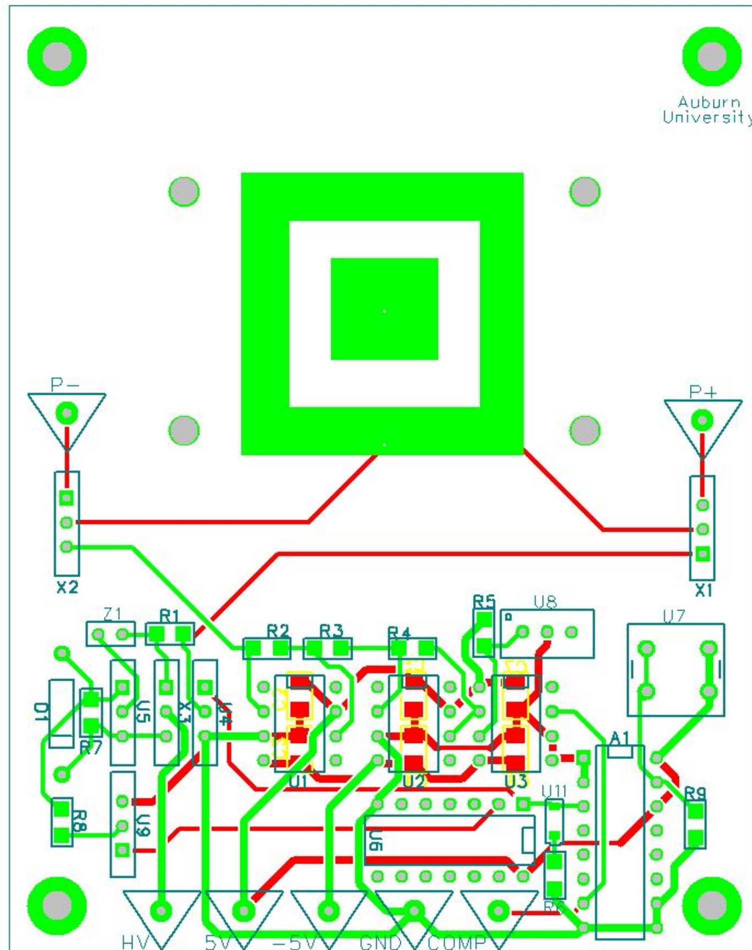

Figure 6.2: Layout of Transimpedance Amplification Circuit.

Figure 6.3 shows the final populated test board used in the experiment. The design completed in figure 6.2 was fabricated by a PCB manufacturer called Advanced Circuits. The PPA is mounted on the PCB using a compression acrylic compression fixture. A plastic spacer of set thickness is placed under the PPA between the board and the device to set

the gap distance between the two electrodes. Another plastic fixture is location stencil to align the device with the plate. Once the device is aligned over the fixed electrode, the compression fixture is tightened with four screws located at each corner of the fixture. The schematic for the acrylic fixture is located in figures E.1 and E.2 of Appendix E Attached to the fixture is a strip of copper conductive tape. This tape facilitated the connection between the upper movable electrode and the detection circuit. As a side note, after a long period of time, both the copper tape and the copper deposited became slightly oxidized which was likely accelerated by high voltage arcing when the electrodes made contact. This oxidation had to be cleaned to maintain reliable device operation.

Figure 6.3: Fabricated Transimpedance Amplification Circuit.

6.2 Results of Test Platform Measurement

The motion of the device was observed using an optical vibrometer and a small reflector attached to the center of the PPA. As the actuator moves, the motion is detected and converted to an electrical voltage with an accuracy of $20\frac{\mu m}{V}$. The device was first tested with the shutdown mechanism of the circuit turned off and a current limiting resistor in series with the actuator. This allowed the actuator to completely snap together to show the full motion of the device, and the behavior of the current up until contact is made. This behavior is shown in figure 6.4. Similar to the Simulink simulation, the current increases when the pull-in condition is achieved, but when the plate makes contact, the current immediately goes to the rail indicating that the device has shorted. The current values gathered experimentally, while similar in magnitude, differ in slope from the Simulink data, particularly when the plates are at their closest. This discrepancy is most likely attributed to the non-idealities not taken into account in the simulation. Squeeze film damping likely reduced the acceleration of the plate at small electrode separation values causing reduced final current. Due to the design of the device meant to reduce the pull-in voltage by making the springs as long as possible, the springs may be slightly nonlinear in different regions of actuation.

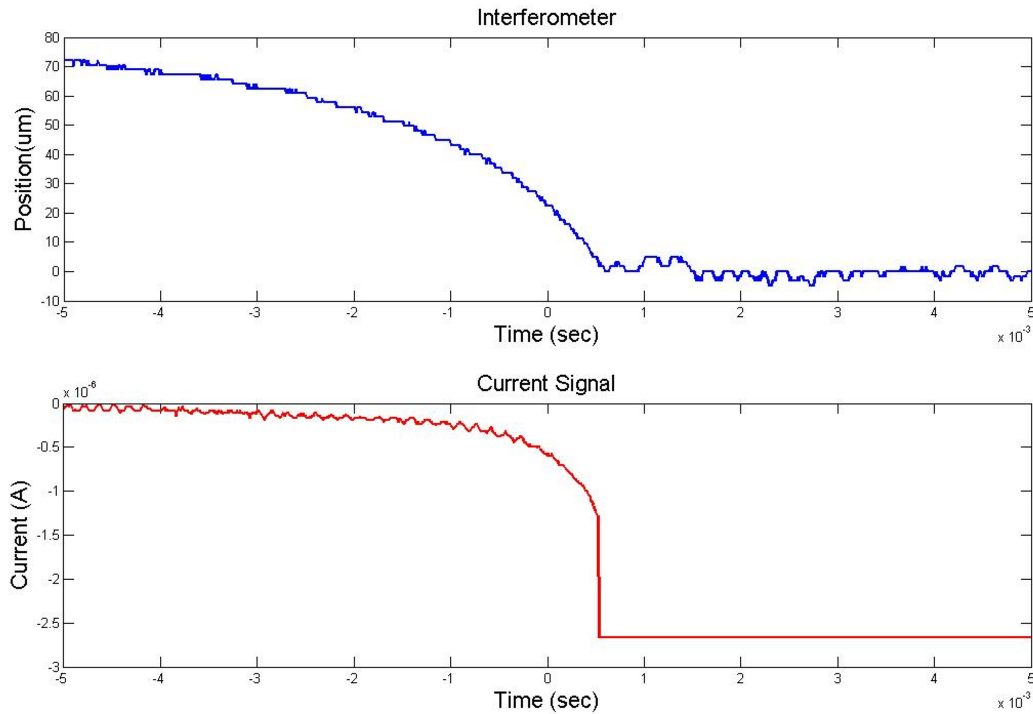

Figure 6.4: Pull-in Event Without Safety Shutdown.

Table 6.1 provides a summary of currents at notable positions during the pull-in process. As shown below, there is about an order of magnitude difference between the simulated and experimental values of pull-in This difference increased as the plated moved closer to contact. This effect could have a number of causes. possible reasons include the following

- The equation 5.1 used to calculate the spring constant is only an approximation, and may not fully account for the springs wrapping around the proof mass which also causes a slight twisting action.
- Resistance in series with the circuit path can hinder current flow causing a slowing in velocity of the PPA.
- Insufficient slew rate of the transimpedance amplifier could cause the signal seen at the output to be lower than the actual value of current passing through the capacitor.

- In order to test the transmissibility of the device, the PPA was placed on a shaker with no bottom electrode attached so that the device would be able to move at many times the magnitude of the input. The lack of a bottom electrode could have caused a reduction in the constant damping that was used in the simulation in comparison to the device when attached to the fixed bottom electrode.

- Similar to the previous item, as the plate moves toward the opposing plate, squeeze film damping would have an increasingly large non-linear effect causing the device to reduce speed dramatically the close it came to contact.

Experimental Current vs. Position		
Distance from Contact	Current (Meas)	Current (Sim)
7.00E-05μm	6.4e-8A	2.50E-07A
4.00E-05μm	2.7e-7A	2.50E-06A
1.00E-05μm	1.03e-6A	4.85E-05A

Table 6.1: Experimental Analysis of Current as a Function of Position

Next, the shutdown mechanism was turned on to test the accuracy and speed at which the voltage could be shut down. A number of trials were run with the comparator voltage set at different levels. Two examples are shown in figures 6.5 and 6.6. In Figure 6.5, the comparator voltage was set to 183mV. Using a gain of 375,000 on the transimpedance amplifier, this voltage should correspond to a current value of 0.488μA. This should equate to a plate position of around 26μm from the opposing plate. In Figure 6.6, the comparator was set to 331mV which corresponds to a current of .882μA and a position of around 12μm. In the two figures, three graphs are presented. The top graph shows the position of the

plate shown by the interferometer. The middle graph shows the moment at which the comparator is tripped. The bottom graph displays the voltage that is present at the output of the transimpedance amplifier which has been converted in Matlab to display the value of the current going through the actuator. All three graphs are synchronized with time. The bottom graph displays a large scale ringing in the current signal at the moment the circuit shuts down. One explanation for this is that when the shutdown mechanism circuit is tripped the inductance in the circuit trace and mosfet that is parallel to the PPA creates an LC tank circuit with high damping resistance that causes the circuit to oscillate while the capacitor discharges. Because this effect occurs after the circuit has been tripped and the actuator returns to its rest-gap position, it can be assumed that this is predominately an electrical effect and has no tangible impact on the mechanical performance of the actuator. The current graphs of both figures verify that the shut-down circuit trips at their appropriate values, and that the actuator immediately rises back to its rest position indicating that the charge has been completely dissipated from the actuator.

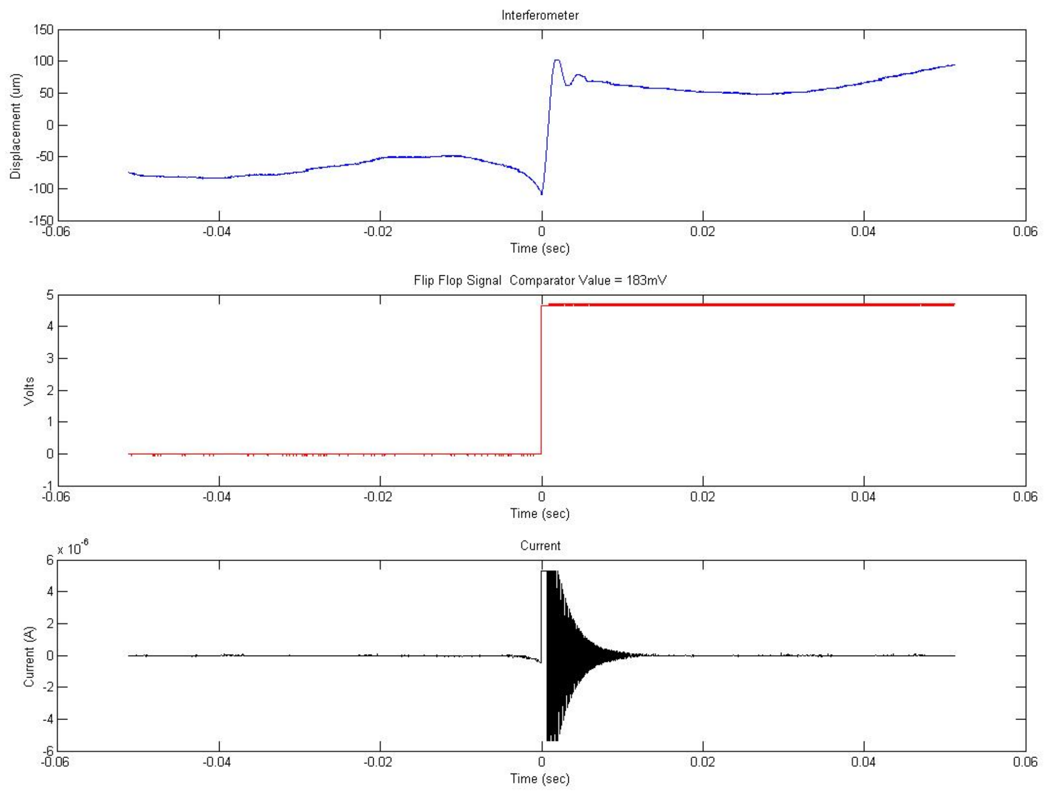

Figure 6.5: Safety Shutdown at 4.88e-7 Amps.

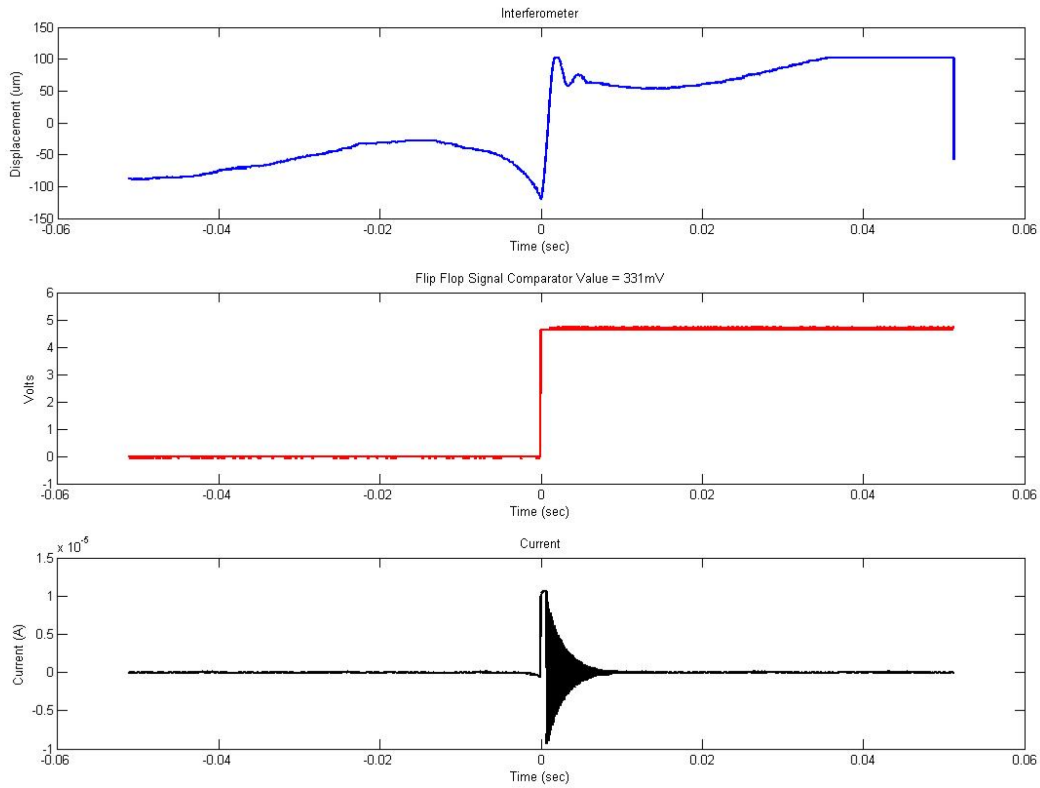

Figure 6.6: PSafety Shutdown at 8.82e-7 Amps.

6.3 Chapter Summary

In this chapter, the process of verifying the simulation developed in chapter 5 is covered. The schematic and layout of the test platform are discussed explaining the operation of the various circuit blocks, including amplification stages, digital control, and safety mechanisms. The final circuit was then evaluated by displaying the electrical output on an oscilloscope and then comparing the data received with the signal from a laser vibrometer directed at the surface of the plate. First the device was allowed to complete the full pull-in event to record the current during the entire process and compare it with the simulated values, It was

found that the current did follow the a trend of exponential increase, but was off by about an order of magnitude. The reasons for this discrepancy were discussed.

By connecting the shut-down mechanism on the circuit, it was then shown that the circuit can indeed respond to the onset of pull-in to prevent the device from making contact. Further, the circuit is fast enough to respond at precise locations during the pull-in event allowing fine grain control over the position the plate will displace beyond the $\frac{1}{3}$ of the rest-gap position. The experimental results showed fairly good correlation with the simulated values in Simulink, with deviation at small gap values that has been predominately attributed to squeeze film damping that has not been added into the simulation.

Chapter 7

Extension of Pull-in Work to Create a Tunable Resonator

While in most cases, the onset of pull-in has detrimental effects, there exist some instances where pull in should be allowed to occur. Some devices are designed to use the pull-in effect in the operation of the device. The pull-in detection method presented here does not only have to be used to halt the onset of pull in but can be used to record that pull-in has occurred or is about to occur. As an example, this detection method may allow a circuit to keep track of the number of times a switch designed on the pull-in principle has become active, and even make changes to the circuit in preparation for the contact event. In an extension to the work on pull-in mitigation, a device was created as explained previously to operate in just this manner. By adding one passive external resistor in series with the PPA previously fabricated a tunable resonator was created that operates on the effect of the charging and discharging actuator when pull-in is completed. The device will resonate at a frequency determined by the value of the resistor by slowing down the charging time of the capacitor in proportion to the resistor value. The mitigation method discussed can be directly applied to this resonator to detect each pull-in event on an on going basis with the addition of a zener diode to protect the input of the transimpedance amplifier. This chapter discusses the design and testing of the resonator structure to show that a stable oscillation occurs over a wide range of frequencies. [51]

7.1 Pull-in Resonator

As discussed previously, if the voltage on the parallel plate actuator increases over a certain value, the system becomes unstable and the plates will snap together. By making both plate surfaces of the PPA conductive and grounding the negative terminal of the actuator, a

short circuit is made when snap-in occurs. Once this happens, the actuator capacitor will be allowed to discharge, thus reducing the voltage across it to zero, allowing the restoring force of the spring to regain control. When the actuator releases, the voltage will immediately increase back to the previous pull-in condition before the mechanical system has time to react. This results in the actuator being locked into place. By placing a very large resistance between the voltage source and the actuator, the current flowing from the voltage source to the actuator can be reduced, increasing the time required to restore the charge on the positive plate of the actuator. If the charge time is sufficiently increased, due to the presence of a large value resistor between the actuator and the power supply, the spring system will then be able to move the actuator away from its snap in position before the voltage between the two plates once again reaches the pull-in condition. Under non-equilibrium conditions, a general description of the force on a parallel plate actuator can be shown by the differential equation shown below where m is the mass of the actuator proof mass, c is a damping coefficient which can be caused by the environment in which the actuator is operating, and k is the spring constant of the system. Figure 7.1 shown below gives an illustration of the mass spring damper system that is described by Figure 7.1.

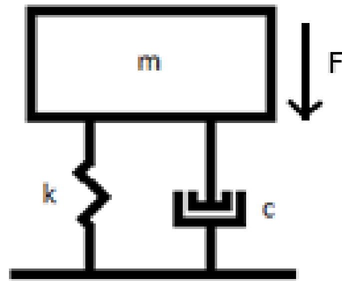

Figure 7.1: Mass Spring Damper System Diagram.

$$\frac{d^2x}{dt^2} + \frac{dx}{dt}c + xk = \frac{V^2\epsilon_o\epsilon_r A}{2\left(x_o - x\right)^2} \tag{7.1}$$

The circuit diagram below shows the resonator system.

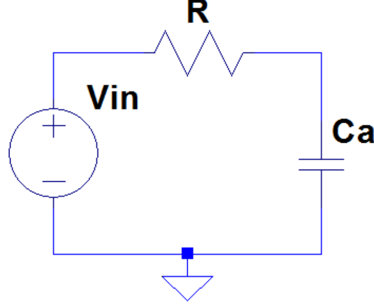

Figure 7.2: Actuator Circuit.

By doing a simple analysis of the circuit in Figure 7.2, the current equation for the current in the circuit can be found, and is shown in the left side of 7.1. Because the capacitance of the actuator is variable, the current into the actuator must be characterized by two components which are shown on the right side of 7.1. The first component is the usual equation for a fixed capacitor where the change in voltage over time causes a current flow. The second component is a result of the change in capacitance over a change in time due to the movement of the actuator. This second component is important, because as the movable plate approaches contact with the fixed plate, the capacitance between the two plates grows enormously. A large series resistance added to the circuit reduces the amount of charge that can flow into the capacitor, which in turn requires that the voltage across the capacitor must drop.

$$I = \frac{V_{in} - V_c}{R} = V_c \frac{dC_a}{dt} + C_a \frac{dV_c}{dt} \tag{7.2}$$

$$\tag{7.3}$$

$$\frac{dV_c}{dt} + V_c \left(\left(\frac{x_o - x}{R\epsilon_o \epsilon_r A} \right) + \frac{dx}{dt} \left(\frac{1}{x_o - x} \right) \right) - \frac{V_{in} \left(x_o - x \right)}{R\epsilon_o \epsilon_r A} = 0 \tag{7.4}$$

By substituting and reorganizing 7.2, yield 7.3, and finally 7.4. The differential equation 7.4 is enough to fully describe the system in Figure 7.2 with the constraint that $x \leq x_o$.

7.2 Pull-in Resonator Simulation

A MATLAB Simulink model of the actuator system was created to confirm the behavior of a parallel plate actuator using various values of resistance to restrict charge flow. In this simulation, the spring system was modeled using the equations presented previously. A constant voltage was maintained which was above the pull-in voltage of the system, while multiple values of resistance impeding the current flow into the actuator were inserted into the circuit to measure the response. Because the voltage was greater than the pull-in voltage of the actuator, the spring moved past the stability point and the plates snapped together. Once the plates shorted, the voltage across the actuator dropped to zero and the charge on the positive plate of the actuator quickly flowed through to the negative plate. Once fully discharged, the two plates then released from each other and began moving apart.

If the resistance between the voltage source and the actuator was low, then the current flow after the plates released was large enough that the charge on the positive plate built back up quickly before the mechanical system had time to respond. The fully charged plates then snapped back together, resulting in an effective permanent snap-in condition.

By increasing the resistance into the Mohm range, the charge time on the positive plate increased enough so that the springs of the actuator have time to respond before the actuator capacitance fully recharged. The actuator plates are able to move a small distance away from each other before the charge built back enough to achieve pull-in voltage again. Once this happened, the actuator returned to its original snap-in condition, creating a periodic cycle of snap-in and release conditions at a frequency that was proportional to the resistance used.

Currently, this simulation is only a general description of the system behavior to show the effect of resistance on a variable capacitance, and is not highly accurate to the specifications of the actual device created for this experiment. A work has been performed on interfacing a PSPICE output to Simulink which has the potential to allow a much more accurate model of the response of the actual fabricated device [52]. In future analysis of the resonator behavior, this technique will be used to model the system. Figure 4 and Figure 5 show

the resonant behavior of the actuator using two different high resistance values. As can be seen in the figure, once snap-in condition is achieved, the high resistance value added to the system causes the actuator to move into an oscillatory state. When the value of resistance is increased, the amplitude of oscillation increased as well, along with a corresponding decrease in frequency due to this extended range of motion.

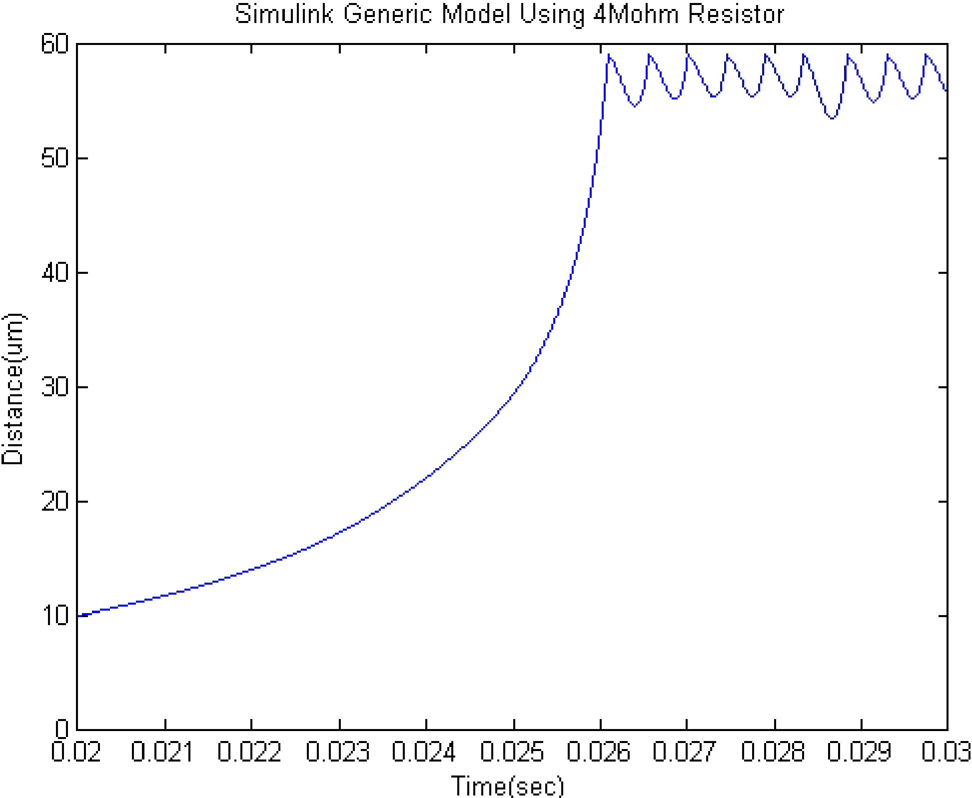

Figure 7.3: Simulink Model Using 4M Resistance.

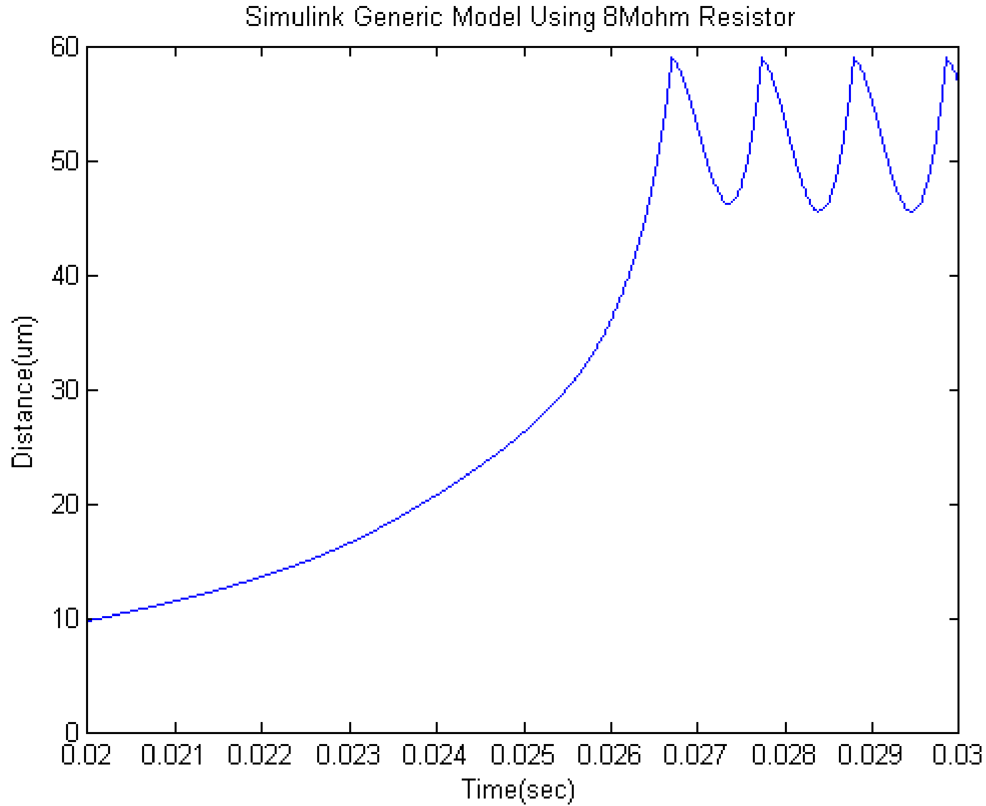

Figure 7.4: Simulink Model Using 8M Resistance.

7.3 Pull-in resonator Experimental Verification

The same PPA test device used to develop the pull-in detection mechanism is used here to create a resonant device. Similarly, the same properties that make this device well suited to detecting the current flow through the actuator make it an ideal device for creating resonance at low frequencies at a suitable voltage range. As shown previously a finite element analysis model of the device in Intellisuite confirmed the following mechanical properties. The primary mode natural frequency though simulation was found to be 248 Hz. Once the device was fabricated, the device was placed on a mechanical shaker to determine the transmissibility curve. The resulting curve showed peak transmissibility at 219.5 Hz, which is relatively close to the simulation prediction. The deviation in frequency was attributed

to simulation assumptions, variations in the material properties, and fabrication tolerances. One consequence of designing a device in such a way that the springs wrap around the device, as in this case, is that in deformation, the mass has a tendency to rotate. Since, in this experiment, displacement is limited to $40\mu m$ this rotation effect was considered negligible. Another effect of the extended spring length is that higher order vibration modes have resonant frequencies only slightly higher than the primary mode. This off-axis movement could cause an unintended reduction in capacitance, as well as cause an imperfect surface contact between the two electrodes when pull-in occurs thereby causing incomplete charge dissipation. While capacitance variation was not found to be a significant source of error, contact quality had a major effect on oscillation reliability. It was determined that off-axis vibration was not the main contributor to the contact quality issue. Contact cleanliness and non-uniform plating of the PCB electrode also played a significant role. When operating with resistances greater than 1M, performing accurate measurements on electrical characteristics can become problematic because the input resistance of many measurement tools is less than the resistance of the system. For this reason, measurement of the displacement of the actuator was performed using an interferometer which affords a non-electrical measurement of the system dynamics.

Figures 7.5,7.6, and 7.7 show the completed components separately and then assembled together. The extra circuitry on the PCB is control circuitry for the actuator that was not used in this investigation.

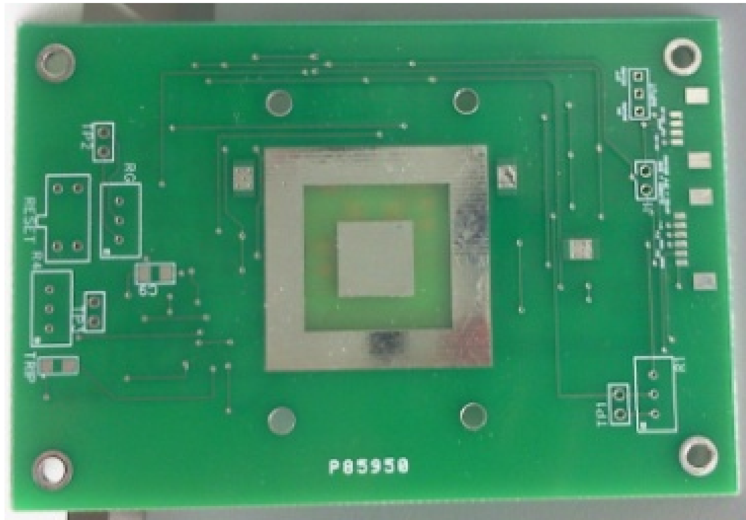

Figure 7.5: PCB Electrode.

Figure 7.6: Fabricated PPA Spring System.

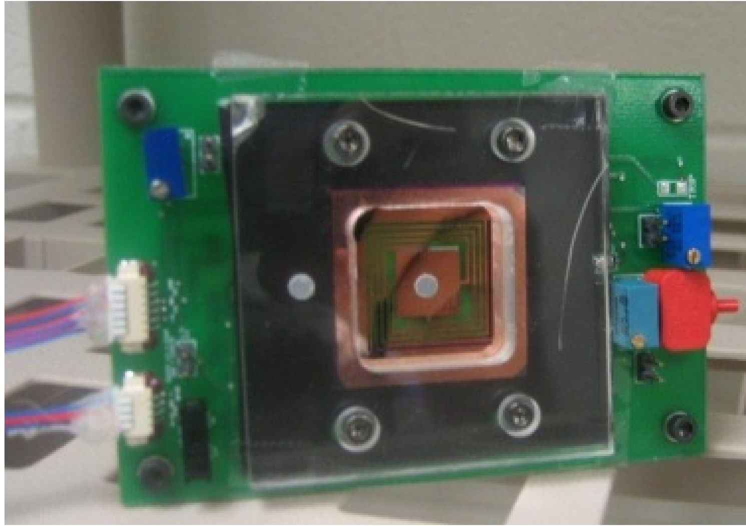

Figure 7.7: Assembled PPA test device.

To test the device, a 400V DC voltage was applied to the circuit. This voltage ensured that the supply voltage remained well above the pull-in voltage of the device. Through experimentation, the measured pull-in voltage was found to be 250V. Varying series resistance values from $21M\Omega$ to $81M\Omega$ in increments of $10M\Omega$ were tested in the circuit. During each test, fairly precise audible oscillation was observed, as well as measured by the interferometer. The oscillations at each frequency is displayed in Figure 7.8. A 60Hz noise signal was also detected in the gathered interferometer data which was removed with post processing of the data in MATLAB. In future experiments, a high-pass filter will be added to the data collection circuitry to reduce this noise. As resistance increased, frequency of oscillation decreased. An FFT analysis was performed on the data in MATLAB, shown in Figure 7.9, to show the movement of the dominant frequency. A frequency shift from 427 Hz down to 146.48 Hz was observed as resistance varied from $21M\Omega$ to 81 $M\Omega$. A displacement of about $2\mu m$ was measured at lower resistances, but only a slight increase in amplitude was observed as the resistance was increased. It may be possible to further increase the amplitude using larger values of resistance.

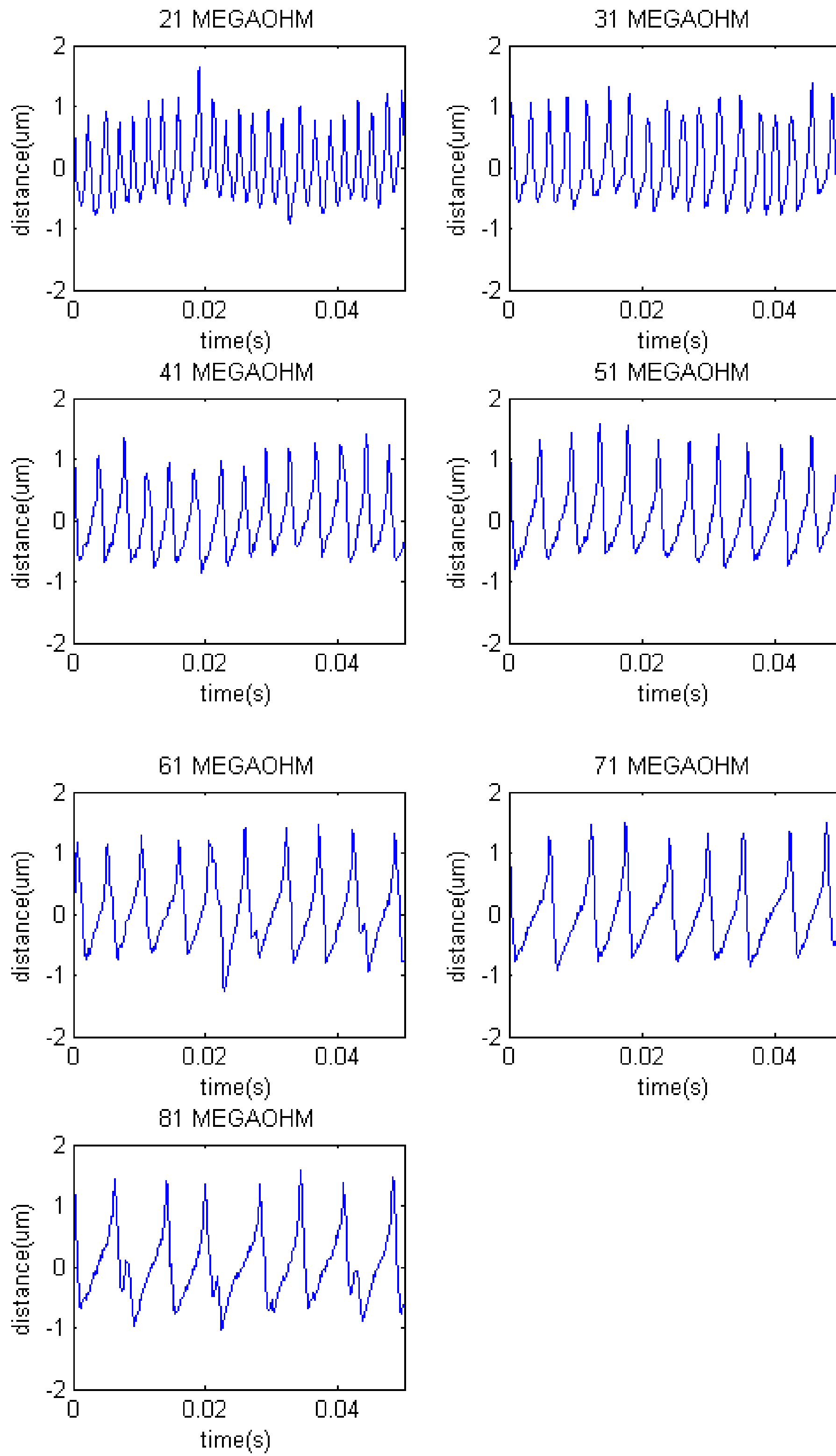

Figure 7.8: Pull-in Oscillations at Various Resistances.

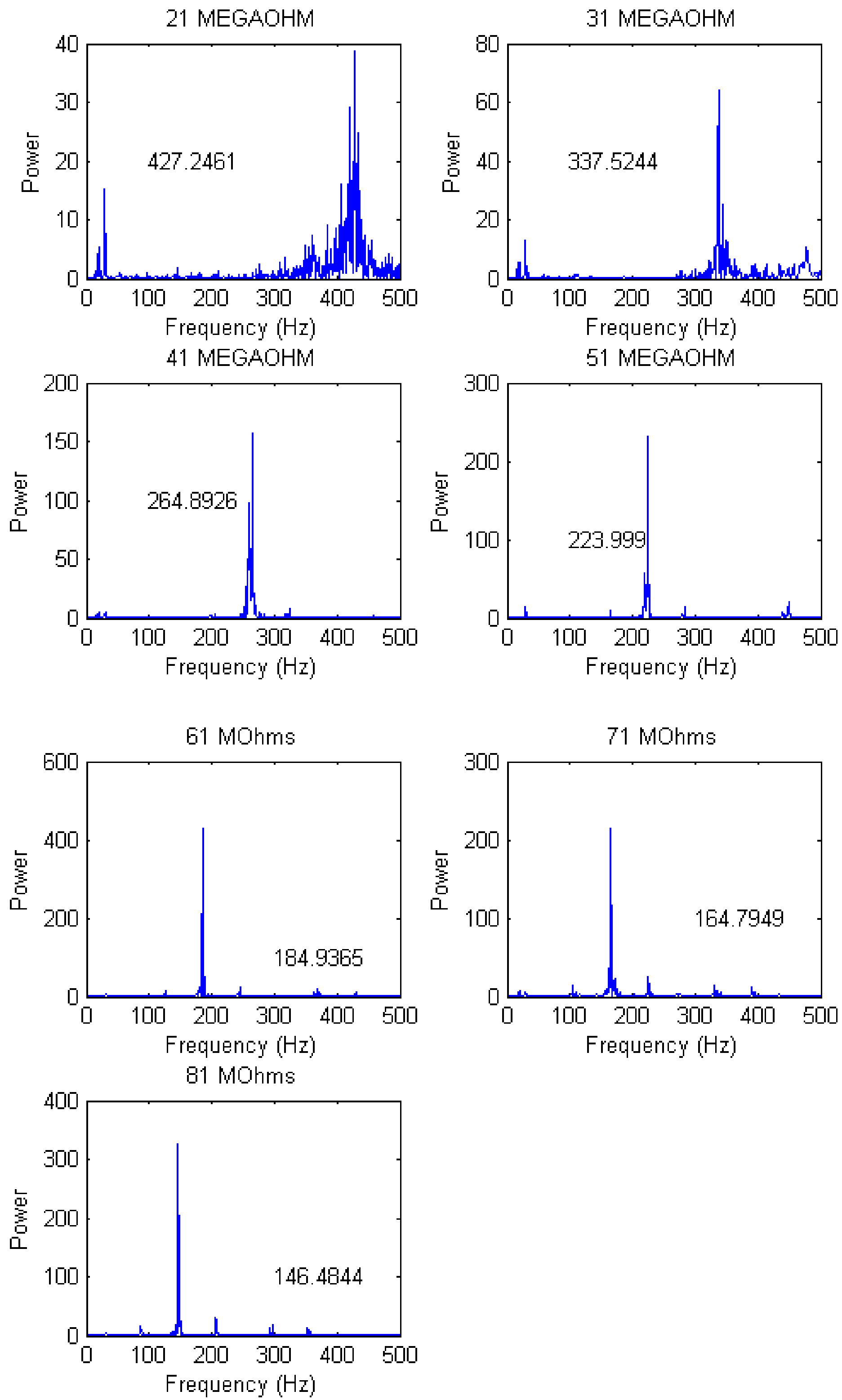

Figure 7.9: FFT Analysis of Pull-in Data .

From the data from Figure 7.9, a definite decreasing trend in frequency was found with increased resistance. By graphing this data in Figure 7.10, this trend can be clearly seen. As the resistance is reduced below 21 M a further increase in frequency is expected. This will also, however, greatly increase the current flow, which if too high results in large power consumption and can damage the device. As a test, a resistance of 30 K was placed into the circuit, and as expected, the plate became stuck in place. The current discharge, however, caused carbon residue to buildup on the surface, degrading the contact quality, and causing unreliable device operation.

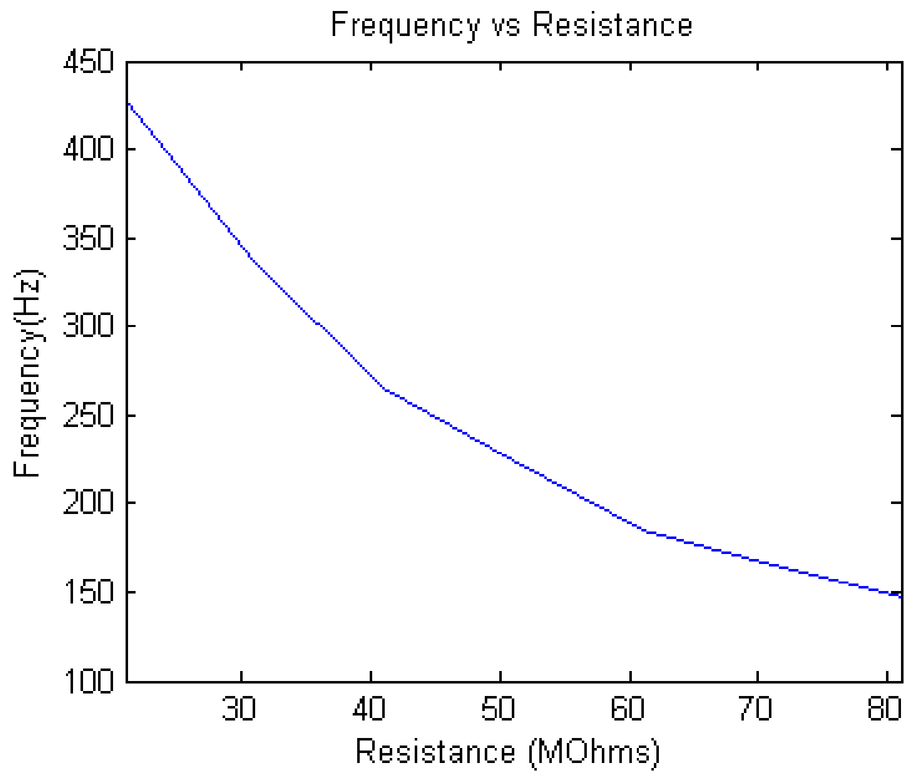

Figure 7.10: Frequency Trend as a Function of Resistance.

7.4 Chapter Summary

By using a high value resistance in series with a parallel plate actuator under snap-in condition, a resonant behavior results in which the device cycles in and out of snap-in.

This behavior occurs at a fairly precise and stable frequency which is controllable by the amount of resistance applied to the circuit. By utilizing the nonlinear behavior inherent in the snap-in condition, a tunable MEMS resonator can be created utilizing a minimum amount of external circuitry. Frequencies between 146Hz and 427Hz were using values of resistance between 21Mohm and 81Mohm. These frequency values are both well below and well above the resonant frequency of the device. Because such high values of resistance were used, there is very little current flow required to actuate the device. Little more than the current required to charge the capacitor is needed to continuously actuate the device, although at higher frequencies, faster charging and discharging cycles will cause more power consumption.

Chapter 8

Conclusions

This work showed through simulation in Simulink and experimentation with a fabricated silicon MEMS structure, that by measuring the current flowing into a parallel plate actuator, the onset of pull-in can be detected by sensing the increased current caused by the rapid increase in capacitance using a fixed voltage source. By creating a model to accurately simulate the PPA motion, the value of the current was predicted to be 1.67nA at the onset of pull-in, then 250nA when the plate reaches approximately 70um from contact, and increasing to 10uA just before the plates make contact. In comparison the experimental results show that when the plate was at 70um from contact the current flowing through the capacitor measured to be 64nA and just before contact, 1.03uA was measured. While the data compares at the same order of magnitude, there is substantial error between the results which increases as the plates move closer to contact. This can be explained by a few factors. First the Simulink model used a constant value for the damping coefficient to resist the motion of the PPA, while in reality motion at close proximity to an opposing plate contributes a non-linear squeeze-film damping term, which opposes the acceleration of the pull-in effect. Another potential source of error can be attributed to unknown resistance in the circuit. While unlikely to cause much change, excessive resistance in the circuit could impede the current flow through the actuator, thus slowing the pull-in. Finally, if the slew rate of the opamp is not sufficiently high, the transimpedance amplifier may not accurately reflect the current flowing through the actuator at high speed. This scenario cannot be ruled out because the amplifier gain was set at or slightly above the maximum gain bandwidth product line of 10MHz in order to produce a measurable signal from the current.

Further, the position of the actuator can be somewhat controlled by associating the speed of the device with the current providing information about the position within the pull-in region. The mitigation event can be delayed until just before the plate makes contact thus preventing damage.

Also as an extension to the work of pull-in detection and mitigation; if the pull-in event is allowed to complete, assuming sufficient circuit protections are in place, and a high value resistor is placed in series with the PPA thereby creating an RC time constant of the same order of magnitude as the resonant frequency of the PPA, the device can be made to resonate with a small displacement. Moreover, as the resistance value is increased, the displacement distance will also increase, and the frequency of the oscillations will decrease proportionally. This behavior was also shown both in simulation and through physical testing. The model created in this simulation only showed a generic behavior of the device and could not, with a high degree of accuracy determine the exact relationship between resistance and frequency of the actual device because of a number of unknown parameters that would be both very difficult to model, and can vary from device to device. A few of these parameters being, motion of the PPA that is not perpendicular to the opposing contact and discharge delay due to corrosion or non-planar electrode surface. The simulation was, however, appropriate for showing the general effects of the charge discharge cycle, specifically, larger displacement and higher frequency motion in relation to varying resistance. In testing, a frequency change from 427Hz to 146Hz was observed with resistances ranging from 21MOhms to 81MOhms. This type of resonator with its simplistic design could have uses in a number of different applications from circuits that operate at a precise frequency, to a sensor that responds to a large scale change in resistance, to generation of an acoustic sound source.

Chapter 9

Future Work

9.1 Pull-in Detection Future Work

The Simulink model can be improved to more accurately reflect the non-linearities of the PPA. The device could be tested in different environments including vacuum. This should allow for a higher Q and reduced squeeze film damping, which should allow the device to more closely follow the simulated results. The device created for this experiment was designed to magnify the motion of the PPA to achieve the largest current possible. By increasing the sensitivity of the detection circuit, this experiment can be scaled down to smaller scale actuators. get high side sensing to work. Fabrication of a laterally actuated PPA on an SOI substrate would allow for a reduction in size and generally more reliable performance. Reducing the size will decrease have offsetting changes to the current signal produced. A reduction in surface area will occur due to the smaller mass in actuation, however, The reduced mass will also allow the device to achieve a higher velocity over a shorter distance, which will increase the $C\frac{dV}{dt}$ term.

This work showed that it is possible to detect the onset of pull-in with a limited ability to determine the position of the plate a given time over the pull-in event. More work can be done fully examining the relationship between current and position, which will give even more precise control over the dynamics of the phenomenon.

Further work would be to implement this system into a larger system to show reliability over a long period of time.

9.2 Pull-in Resonator Future Work

The device has so far not been tested under vacuum conditions. This should result in an increase in amplitude at the same resistance value by reducing the damping coefficient. Secondly, because the current device was created emphasizing ease of use, a frequency increase can be achieved by creating a physically smaller version of the actuator. Because contact quality was an issue in this experiment, utilizing an SOI design process for the miniaturized version would minimize the amount of manual positioning currently required, which was a major source of error.

Bibliography

[1] A. Sundaram, M. Maddela, R. Ramadoss, and L. Feldner, “MEMS-Based electronically steerable antenna array fabricated using PCB technology,” *Microelectromechanical Systems, Journal of*, vol. 17, no. 2, pp. 356 –362, Apr. 2008.

[2] C.-H. Han, D.-H. Choi, and J.-B. Yoon, “Parallel-plate MEMS variable capacitor with superior linearity and large tuning ratio using a levering structure,” *Microelectromechanical Systems, Journal of*, vol. 20, no. 6, pp. 1345 –1354, Dec. 2011.

[3] M. Kraft, C. Lewis, T. Hesketh, and S. Szymkowiak, “A novel micromachined accelerometer capacitive interface,” *Sensors and Actuators A: Physical*, vol. 68, no. 13, pp. 466–473, Jun. 1998. [Online]. Available: http://www.sciencedirect.com/science/article/pii/S0924424798000648

[4] S. J. Kim, G. Flowers, C. Chen, and R. Dean, “Active vibration control and isolation for micro-machined devices,” in *ASME 2008 Conference on Smart Materials, Adaptive Structures and Intelligent Systems*, Jan. 2008, pp. 657–664. [Online]. Available: http://dx.doi.org/10.1115/SMASIS2008-423

[5] S. M. Wentworth, *Applied Electromagnetics : Early Transmission Lines Approach*, 1st ed. Wiley, Jan. 2007.

[6] V. Kaajakari, *Practical MEMS: Design of microsystems, accelerometers, gyroscopes, RF MEMS, optical MEMS, and microfluidic systems.* Small Gear Publishing, Mar. 2009.

[7] Y. Nemirovsky and O. Bochobza-Degani, “A methodology and model for the pull-in parameters of electrostatic actuators,” *Journal of Microelectromechanical Systems*, vol. 10, no. 4, pp. 601–615, 2001.

[8] J. I. Seeger and B. E. Boser, “Dynamics and control of parallel-plate actuators beyond the electrostatic instability,” in *Transducers*, vol. 99, 1999, p. 474477.

[9] A. Nayfeh, M. Younis, and E. Abdel-Rahman, “Dynamic pull-in phenomenon in MEMS resonators,” *Nonlinear Dynamics*, vol. 48, no. 1, pp. 153–163, 2007. [Online]. Available: http://www.springerlink.com/content/23228w234n10h5j8/abstract/

[10] J. Seeger and B. Boser, “Charge control of parallel-plate, electrostatic actuators and the tip-in instability,” *Journal of Microelectromechanical Systems*, vol. 12, no. 5, pp. 656 – 671, Oct. 2003.

[11] J. Yao and M. Chang, "A surface micromachined miniature switch for telecommunications applications with signal frequencies from DC up to 4 ghz," in *Solid-State Sensors and Actuators, 1995 and Eurosensors IX.. Transducers '95. The 8th International Conference on*, vol. 2, Jun. 1995, pp. 384 –387.

[12] G. Rebeiz and J. B. Muldavin, "RF MEMS switches and switch circuits," *IEEE Microwave Magazine*, vol. 2, no. 4, pp. 59–71, 2001.

[13] S. Pacheco, L. P. B. Katehi, and C. Nguyen, "Design of low actuation voltage RF MEMS switch," in *Microwave Symposium Digest. 2000 IEEE MTT-S International*, vol. 1, 2000, pp. 165–168 vol.1.

[14] J. B. Muldavin and G. Rebeiz, "High-isolation CPW MEMS shunt switches. 1. modeling," *IEEE Transactions on Microwave Theory and Techniques*, vol. 48, no. 6, pp. 1045–1052, 2000.

[15] J. Xie, J. Shih, Q. Lin, B. Yang, and Y.-C. Tai, "Surface micromachined electrostatically actuated micro peristaltic pump," *Lab on a Chip*, vol. 4, no. 5, p. 495, 2004. [Online]. Available: http://pubs.rsc.org/en/Content/ArticleLanding/2004/LC/b403906h

[16] J. Seeger and S. Crary, "Stabilization of electrostatically actuated mechanical devices," in *Solid State Sensors and Actuators, 1997. TRANSDUCERS '97 Chicago., 1997 International Conference on*, vol. 2, Jun. 1997, pp. 1133 –1136 vol.2.

[17] X. Wu, Z. Xiao, J. Zhe, and K. Farmer, "Modeling and simulation of two passive feedback methods to obtain large travel range of electrostatic micro mirrors," in *Proceedings of 4th international conference on modeling and simulation of microsystems, Hilton Head, SC*, 2001, p. 1921.

[18] R. Nadal-Guardia, A. Dehe, R. Aigner, and L. Castaner, "Current drive methods to extend the range of travel of electrostatic microactuators beyond the voltage pull-in point," *Journal of Microelectromechanical Systems*, vol. 11, no. 3, pp. 255–263, 2002.

[19] R. Legtenberg, J. Gilbert, S. Senturia, and M. Elwenspoek, "Electrostatic curved electrode actuators," *Microelectromechanical Systems, Journal of*, vol. 6, no. 3, pp. 257 –265, Sep. 1997.

[20] J. Zhe, X. Wu, J. Cheng, J. Wang, K. Farmer, L. Frechette, and V. Modi, "Analytic pull-in study on non-deformable electrostatic micro actuators," in *Technical Proceedings of the 2002 International Conference on Modeling and Simulation of Microsystems*, 2002.

[21] J. Seeger and B. Boser, "Negative capacitance for control of gap-closing electrostatic actuators," in *TRANSDUCERS, Solid-State Sensors, Actuators and Microsystems, 12th International Conference on, 2003*, vol. 1, Jun. 2003, pp. 484 – 487 vol.1.

[22] M. Lu and G. Fedder, "Position control of parallel-plate microactuators for probe-based data storage," *Journal of Microelectromechanical Systems*, vol. 13, no. 5, pp. 759–769, 2004.

[23] E. Hung and S. Senturia, "Extending the travel range of analog-tuned electrostatic actuators," *Journal of Microelectromechanical Systems*, vol. 8, no. 4, pp. 497 –505, Dec. 1999.

[24] R. Dean, C. Wilson, J. Brunsch, and J. Hung, "A synthetic voltage division controller to extend the stable operating range of parallel plate actuators," in *Control Applications (CCA), 2011 IEEE International Conference on*, Sep. 2011, pp. 1068 –1074.

[25] L. Mol, R. Wolffenbuttel, E. Cretu, and L. Rocha, "Full-gap positioning of parallel-plate electrostatic MEMS using on-off control," in *Industrial Electronics, 2007. ISIE 2007. IEEE International Symposium on*, Jun. 2007, pp. 1464 –1468.

[26] M. Semiconductor, "Application note 746: High-side current-sense measurement: Circuits and principles." [Online]. Available: http://pdfserv.maxim-ic.com/en/an/AN746.pdf

[27] H. Forghani-zadeh and G. Rincon-Mora, "Current-sensing techniques for DC-DC converters," in *The 2002 45th Midwest Symposium on Circuits and Systems, 2002. MWSCAS-2002*, vol. 2, 2002, pp. II–577–II–580 vol.2.

[28] T. Regan, "Current sense circuit collection," Dec. 2005. [Online]. Available: http://cds.linear.com/docs/Application%20Note/an105.pdf

[29] G. Ferrari, F. Gozzini, A. Molari, and M. Sampietro, "Transimpedance amplifier for high sensitivity current measurements on nanodevices," *IEEE Journal of Solid-State Circuits*, vol. 44, no. 5, pp. 1609–1616, 2009.

[30] C. Xiao, L. Zhao, T. Asada, W. Odendaal, and J. Van Wyk, "An overview of integratable current sensor technologies," in *Industry Applications Conference, 2003. 38th IAS Annual Meeting. Conference Record of the*, vol. 2, 2003, pp. 1251–1258 vol.2.

[31] P. A. Roos, M. Stephens, and C. E. Wieman, "Laser vibrometer based on optical-feedback-induced frequency modulation of a single-mode laser diode," *Applied Optics*, vol. 35, no. 34, pp. 6754–6761, Dec. 1996. [Online]. Available: http://ao.osa.org/abstract.cfm?URI=ao-35-34-6754

[32] A. Wisitsoraat, V. Patthanasetakul, T. Lomas, and A. Tuantranont, "Low cost thin film based piezoresistive MEMS tactile sensor," *Sensors and Actuators A: Physical*, vol. 139, no. 12, pp. 17–22, Sep. 2007. [Online]. Available: http://www.sciencedirect.com/science/article/pii/S0924424706006510

[33] T.-R. Hsu, *MEMS & Microsystems: Design, Manufacture, and Nanoscale Engineering.* John Wiley & Sons, Mar. 2008.

[34] Z. Xiao, W. Peng, R. F. Wolffenbuttel, and K. R. Farmer, "Micromachined variable capacitors with wide tuning range," *Sensors and Actuators A: Physical*, vol. 104, no. 3, pp. 299 – 305, 2003, <ce:title>Selected papers based on contributions revised from the Technical Digest of the 2002 Solid-State

Sensors, Actuators and Microsystems workshop</ce:title>. [Online]. Available: http://www.sciencedirect.com/science/article/pii/S0924424703000487

[35] B. Mammano, "Current sensing solutions for power supply designers," in *Unitrode Seminar Notes SEM1200*, 1999.

[36] S. J. Kim, "An evaluation system for mechanical and electrical characterization of MEMS devices," Thesis, Auburn University, May 2009. [Online]. Available: http://etd.auburn.edu/etd/handle/10415/1592

[37] R. C. Jaeger, *Introduction to Microelectronic Fabrication: Volume 5 of Modular Series on Solid State Devices*, 2nd ed. Prentice Hall, Oct. 2001.

[38] R. Hull, *Properties of Crystalline Silicon*. IET, 1999.

[39] P. V. Zant, *Microchip fabrication*. McGraw-Hill Professional, 2004.

[40] S. Linder, H. Baltes, F. Gnaedinger, and E. Doering, "Photolithography in anisotropically etched grooves," in *IEEE, The Ninth Annual International Workshop on Micro Electro Mechanical Systems, 1996, MEMS '96, Proceedings. An Investigation of Micro Structures, Sensors, Actuators, Machines and Systems*, 1996, pp. 38–43.

[41] N. Layadi, V. M. Donnelly, and J. T. C. Lee, "Cl[sub 2] plasma etching of si(100): Nature of the chlorinated surface layer studied by angle-resolved x-ray photoelectron spectroscopy," *Journal of Applied Physics*, vol. 81, no. 10, p. 6738, 1997. [Online]. Available: http://link.aip.org/link/JAPIAU/v81/i10/p6738/s1&Agg=doi

[42] D. M. Manos, *Plasma etching*. Academic Press, 1989.

[43] H. Zou, "Anisotropic si deep beam etching with profile control using SF 6/O 2 plasma," *Microsystem Technologies*, vol. 10, no. 8, p. 603607, Nov. 2004. [Online]. Available: http://dx.doi.org/10.1007/s00542-003-0338-3

[44] J. Hopwood, "Review of inductively coupled plasmas for plasma processing," *Plasma Sources Science Technology*, vol. 1, p. 109116, May 1992. [Online]. Available: http://adsabs.harvard.edu/abs/1992PSST....1..109H

[45] F. Laermer and A. Schilp, "Method of anisotropically etching silicon," U.S. Patent 5 501 893, Mar., 1996. [Online]. Available: http://patft.uspto.gov/netacgi/nph-Parser?Sect1=PTO1&Sect2=HITOFF&d=PALL&p=1&u=%2Fnetahtml%2FPTO%2Fsrchnum.htm&r=1&f=G&l=50&s1=5501893.PN.&OS=PN/5501893&RS=PN/5501893

[46] F. Marty, L. Rousseau, B. Saadany, B. Mercier, O. Franais, Y. Mita, and T. Bourouina, "Advanced etching of silicon based on deep reactive ion etching for silicon high aspect ratio microstructures and three-dimensional micro- and nanostructures," *Microelectronics Journal*, vol. 36, no. 7, p. 673677, Jul. 2005. [Online]. Available: http://www.sciencedirect.com/science/article/B6V44-4GBD718-1/2/70c45f3f91afaa974b5a88fcfc274f32

[47] M. Wasilik and A. P. Pisano, “Low-frequency process for silicon-on-insulator deep reactive ion etching,” in *Device and Process Technologies for MEMS and Microelectronics II*, J.-C. Chiao, L. Faraone, H. B. Harrison, and A. M. Shkel, Eds., vol. 4592. Adelaide, Australia: SPIE, Nov. 2001, p. 462472. [Online]. Available: http://link.aip.org/link/?PSI/4592/462/1

[48] N. Roxhed, P. Griss, and G. Stemme, “A method for tapered deep reactive ion etching using a modified bosch process,” *Journal of Micromechanics and Microengineering*, vol. 17, no. 5, p. 10871092, 2007. [Online]. Available: http://iopscience.iop.org/0960-1317/17/5/031

[49] A. A. Ayn, X. Zhang, and R. Khanna, “Ultra deep anisotropic silicon trenches using deep reactive ion etching (DRIE),” in *Proceedings of the 2000 Solid State Sensors and Actuator Workshop*, Hilton Head, SC, USA, Jun. 2000, p. 339342.

[50] M. J. Madou, *Fundamentals of Microfabrication: The Science of Miniaturization, Second Edition*, 2nd ed. CRC Press, Mar. 2002.

[51] C. Stevens, C. Wilson, and R. Dean, “Micromachined snap-in resonators,” in *International Microelectronics and Packaging Society Device Packaging Conference 2012*, Scottsdale/Fountain Hills, Arizona, 2012.

[52] C. Wilson and J. Hung, “A system simulation technique combining SPICE and SIMULINK tools,” in *IECON 2010 - 36th Annual Conference on IEEE Industrial Electronics Society*, 2010, pp. 41–46.

Appendices

Appendix A

PPA Traveller

I. RCA Clean

1. A Clean
   (a) Acetone Bath 1 minute
   (b) DI water Rinse 1 minute
   (c) IPA bath 1 minute
   (d) Di water Rinse 1 Minute
2. B Clean
   (a) 5-1-1 mixture 5 : $DI\ H_2O$ 1 : 30% H_2O_2 1 : 29% NH_4OH heated to 70° for 5 Minutes
   (b) DI water Rinse 1 Minute
3. C Clean
   (a) HF bath for 30 Seconds
   (b) DI water Rinse 1 Minute
   (c) Second DI water Rinse for 1 Minute

II. Spin Rinse Dryer

III. Dehydration Bake

IV. Photolithography

1. Deposit HMDS Vapor

(a) Temperature: Room Temperature

(b) Time: 5 Minutes

2. Spin Photoresist

(a) Photoresist:AZ4620

(b) Speed:2500RPM

(c) Ramp Speed: 450 R/sec

(d) Time: 45sec

(e) Expected Thickness: $7\mu m$

3. Soft Bake

(a) Temp: $110°C$

(b) Time:4 Minutes (Longer Bake Time to prevent Bubble Formation)

4. UV Exposure

(a) Channel 2 (275 Watts)

(b) Exposure Type: Hard

(c) Cycles: 3

(d) Exposure Time: 10 seconds with 20 seconds wait time

5. Pattern Development

(a) Developer: AZ400

(b) Mixture: 3 parts DI Water to 1 Part Developer

(c) Time: 2 Minutes with agitation

V. Inspect Pattern In 5 places to ensure complete development.

VI. Descum

1. Power: 300W

2. Time: 15 Seconds

VII. Backing wafer Application

1. Spin photoresist

   (a) Photoresist:AZ5214

   (b) Speed:1000RPM

   (c) Ramp Speed: 300 R/sec

   (d) Time: 9sec

   (e) Expected Thickness: $3\mu m$

2. Attach SOI wafer to backing wafer device layer side down

3. Soft Bake

   (a) Temp:$100°C$

   (b) Time:3 Minutes

VIII. DRIE

(a) Program:MORGNSOI

(b) 400 cycles or until backing wafer is exposed

IX. Backing Wafer and Photoresist Removal

(a) Acetone Bath

(b) Isoproponal Bath

(c) DI Water Bath

(d) Weak Piranha Clean

   i. 4 parts H_2SO_4 1 part H_2O_2

   ii. Let solution stand for 5 minutes to cool to $70°C$

iii. time: 5 minutes

iv. 1 minute DI Water Bath

v. Isoproponal Bath

(e) Separate individual devices from wafer

X. Front Side Metallization

(a) Mount devices on Supporting wafer

(b) Argon Ion Abasement: 5 Minutes

(c) Metal Composition: 1000ÅTi, 4000ÅCu

XI. Backside Metallization

(a) remove devices from front side supporting wafer

(b) flip devices and mount again on supporting wafer Supporting wafer

(c) Argon Ion Abasement: 5 Minutes

(d) Metal Composition: 1000ÅTi, 4000ÅCu

Appendix B

Electron Beam Metal Deposition

Table B.1: Electron Beam Metal Deposition Recipe

Ion Beam Parameters	
Pressure	1×10^{-6} Torr
Ion Beam Duration	3 minutes
Ion Beam Cathode Current	6.46 Amps
Ion Beam Discharge Voltage	2.78 Volts
Ion Beam Current	205 Amps
Ion Acceleration Current	4 Amps
Neu emission Current	264
Electron Beam General Parameters	
Discharge Voltage	55.1
Acceleration Voltage	102
Filament Current	5.12 Amps
Layer Index	3

Appendix C

Listing of Lab Equipment by Room#/Laboratory

- **Room # 455-461 Microfabrication Laboratory**
  - STI Semitool 200 Spin Rinse Dryer
  - Tencor Alpha-Step 200 Profilometer
  - Imperial IV Ultra-Clean 100 Dehydration Oven
  - Blue M OTP-120 Dehydration Oven
  - Tousimis Samdry PVT-3D Critical Point Dryer
  - CHA-Industries Mark 50 E-beam/Sputter System
  - Thermco 4000 Horizontal Tube Oxidation Furnace
  - Prometrix SpectraMap FT750 and Prometrix SpectraMap SM200/e
  - Karl Suss MA6/BA6 Contact Mask Aligner
  - Nikon 203338 High Magnification Microscope
  - Olympus SZ-PT Zoom Stereo Microscope
  - Matrix System One Oxygen Plasma Etcher Style 303
  - CEE Spin Coater
  - Hot Plate
  - YES 450-PB8-2P-CP Vacuum Bake Oven
  - YES 5 Dry Vacuum Bake Oven
  - STS Multiplex ICP Advanced Silicon Etcher

- Dicing Machine
- UV Flood Exposure System
- Branson 5510 Ultrasonic Shaker

- **Room# 466 MEMS Testing Lab Room#**
  - Micro-manipulator Manual Probe Station
  - HP 4156A Precision Semiconductor Parameter Analyzer

- **Room# 103 Laboratory for Electronics Assembly and Packaging**
  - Sonix C mode Scanning Acoustic Microscope
  - Nikon Measurescope MM-11 with Quadra-Check 2000 Measurement System

- **Room# 464 Advanced Packaging Print and Fire Laboratory**
  - Buehler Automatic Grinder/Polisher
  - Buehler VibroMet Vibratory Polisher
  - Low Power Microscope
  - Digital Scale

Appendix D

Matlab Code used to Analyze Interferometer Data

```
clear all; clc;
M=dlmread('21meg.csv',',',2,0);
meg21=M; clear M
M=dlmread('31meg.csv',',',2,0);
meg31=M; clear M
M=dlmread('41meg.csv',',',2,0);
meg41=M; clear M
M=dlmread('51meg.csv',',',2,0);
meg51=M; clear M
M=dlmread('61meg.csv',',',2,0);
meg61=M; clear M
M=dlmread('71meg.csv',',',2,0);
meg71=M; clear M
M=dlmread('81meg.csv',',',2,0);
meg81=M; clear M
M=dlmread('91meg.csv',',',2,0);
meg91=M; clear M
%Simple Low-Pass Filter
f=10000
fNorm = 70 / (f/2);
[b,a] = butter(2, fNorm, 'high');
%Apply Filter
fmeg21 = filter(b,a,meg21(:,2))*20;
fmeg31 = filter(b,a,meg31(:,2))*20;
fmeg41 = filter(b,a,meg41(:,2))*20;
```

```
fmeg51 = filter(b,a,meg51(:,2))*20;
fmeg61 = filter(b,a,meg61(:,2))*20;
fmeg71 = filter(b,a,meg71(:,2))*20;
fmeg81 = filter(b,a,meg81(:,2))*20;
fmeg91 = filter(b,a,meg91(:,2))*20;
%filter(a, [1 a-1], x);

fs = 10000;                          % Sample frequency (Hz)
t = 0:1/fs:10-1/fs;                % 10 sec sample
% x = (1.3)*sin(2*pi*15*t) ...       % 15 Hz component
%   + (1.7)*sin(2*pi*40*(t-2)) ...   % 40 Hz component
%   + (2.5)*randn(size(t));          % Gaussian noise;


m = length(fmeg51);           % Window length
n = pow2(nextpow2(m));  % Transform length
           % DFT
f = (0:n-1)*(fs/n);     % Frequency range


figure(1);subplot(2,2,1);
plot(meg21(:,1),fmeg21); title('21 MEGAOHM');xlim([0 0.05]);
ylim([-2 2]); ylabel('distance(um)');xlabel('time(s)');
figure(2);subplot(2,2,1);
y = fft(fmeg21,n); power = y.*conj(y)/n;
[C,I] = max(power);  % Power of the DFT
plot(f,power); xlim([0 500]);xlabel('Frequency (Hz)');
ylabel('Power'); title('21 MOhms');text(100,20,num2str(f(I)))
freqplot(1,:) =[21,f(I)];

figure(1);subplot(2,2,2)
%figure(2)
plot(meg31(:,1),fmeg31); title('31 MEGAOHM');xlim([0 0.05]);
```

```
ylim([-2 2]);ylabel('distance(um)');xlabel('time(s)');
figure(2);subplot(2,2,2);
y = fft(fmeg31,n); power = y.*conj(y)/n;
[C,I] = max(power);  % Power of the DFT
plot(f,power); xlim([0 500]);xlabel('Frequency (Hz)'); ylabel('Power');
title('31 MOhms');text(100,40,num2str(f(I)))
freqplot(2,:) =[31,f(I)];

figure(1);subplot(2,2,3)
%figure(3)
plot(meg41(:,1),fmeg41); title('41 MEGAOHM');xlim([0 0.05]); ylim([-2 2]);
ylabel('distance(um)');xlabel('time(s)');
figure(2);subplot(2,2,3);
y = fft(fmeg41,n); power = y.*conj(y)/n;
[C,I] = max(power);  % Power of the DFT
plot(f,power); xlim([0 500]);xlabel('Frequency (Hz)');
ylabel('Power'); title('41 MOhms');text(100,100,num2str(f(I)))
freqplot(3,:) =[41,f(I)];



figure(1);subplot(2,2,4)
%figure(4)
plot(meg51(:,1),fmeg51); title('51 MEGAOHM');xlim([0 0.05]);
ylim([-2 2]);ylabel('distance(um)');xlabel('time(s)');
figure(2);subplot(2,2,4);
y = fft(fmeg51,n); power = y.*conj(y)/n;
[C,I] = max(power);  % Power of the DFT
plot(f,power); xlim([0 500]);xlabel('Frequency (Hz)');
ylabel('Power'); title('51 MOhms');text(100,100,num2str(f(I)))
freqplot(4,:) =[51,f(I)];

figure(3);subplot(2,2,1)
%figure(5)
```

```
plot(meg61(:,1),fmeg61); title('61 MEGAOHM');xlim([0 0.05]);
ylim([-2 2]);ylabel('distance(um)');xlabel('time(s)');
figure(4);subplot(2,2,1);
y = fft(fmeg61,n); power = y.*conj(y)/n;
[C,I] = max(power);  % Power of the DFT
plot(f,power); xlim([0 500]);xlabel('Frequency (Hz)');
ylabel('Power'); title('61 MOhms');text(300,100,num2str(f(I)))
freqplot(5,:) =[61,f(I)];

figure(3);subplot(2,2,2)
%figure(6)
plot(meg71(:,1),fmeg71); title('71 MEGAOHM');xlim([0 0.05]);
ylim([-2 2]);ylabel('distance(um)');xlabel('time(s)');
figure(4);subplot(2,2,2);
y = fft(fmeg71,n); power = y.*conj(y)/n;
[C,I] = max(power);   % Power of the DFT
plot(f,power); xlim([0 500]);xlabel('Frequency (Hz)');
ylabel('Power'); title('71 MOhms');text(300,100,num2str(f(I)))
freqplot(6,:) =[71,f(I)];

figure(3);subplot(2,2,3)
%figure(7)
plot(meg81(:,1),fmeg81); title('81 MEGAOHM');xlim([0 0.05]);
ylim([-2 2]);ylabel('distance(um)');xlabel('time(s)');
figure(4);subplot(2,2,3);
y = fft(fmeg81,n); power = y.*conj(y)/n;
[C,I] = max(power);   % Power of the DFT
plot(f,power); xlim([0 500]);xlabel('Frequency (Hz)');
ylabel('Power'); title('81 MOhms');text(300,100,num2str(f(I)))
freqplot(7,:) =[81,f(I)];

figure(5);
plot(freqplot(:,1),freqplot(:,2));
```

```
title('Frequency vs Resistance');xlabel('Resistance (MOhms)');
ylabel('Frequency(Hz)');
xlim([21 81])
```

Appendix E

Schematic Drawing of PPA Board Mount Fixture

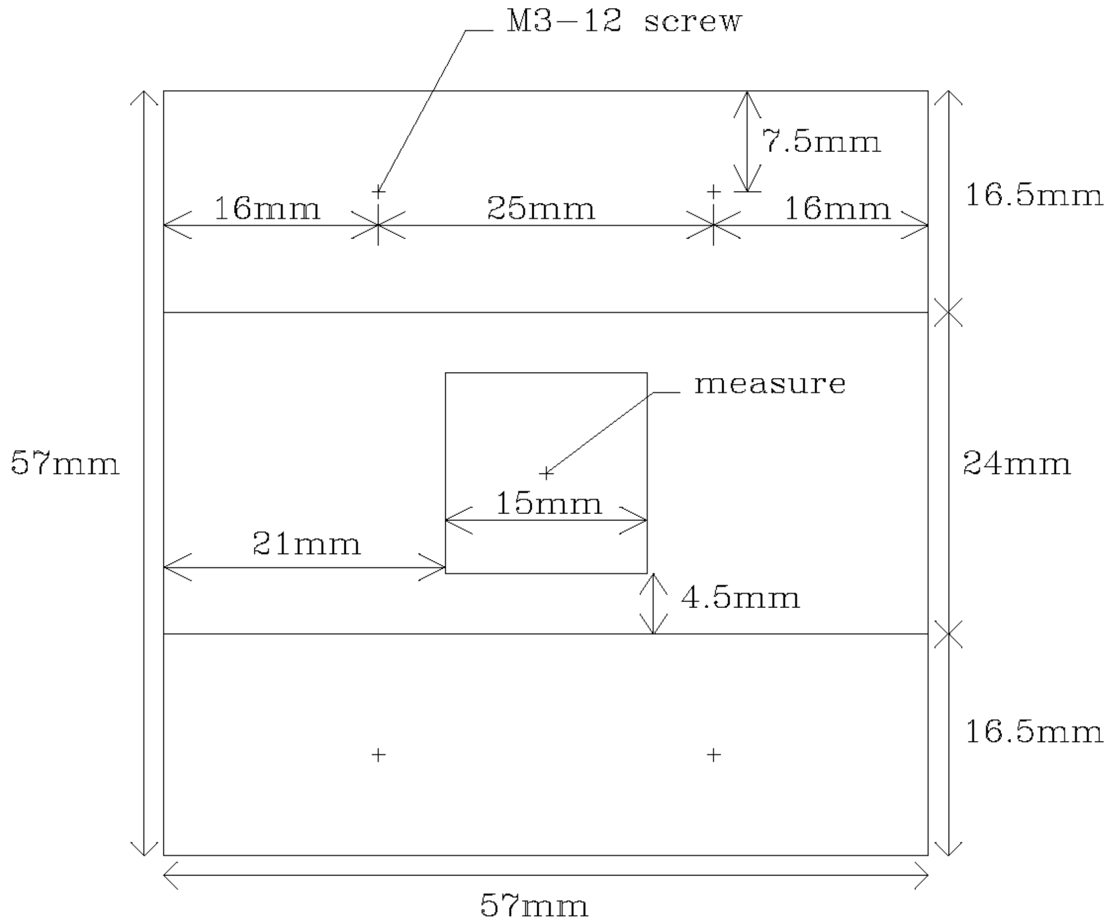

Figure E.1: Bottom of fixture Design.

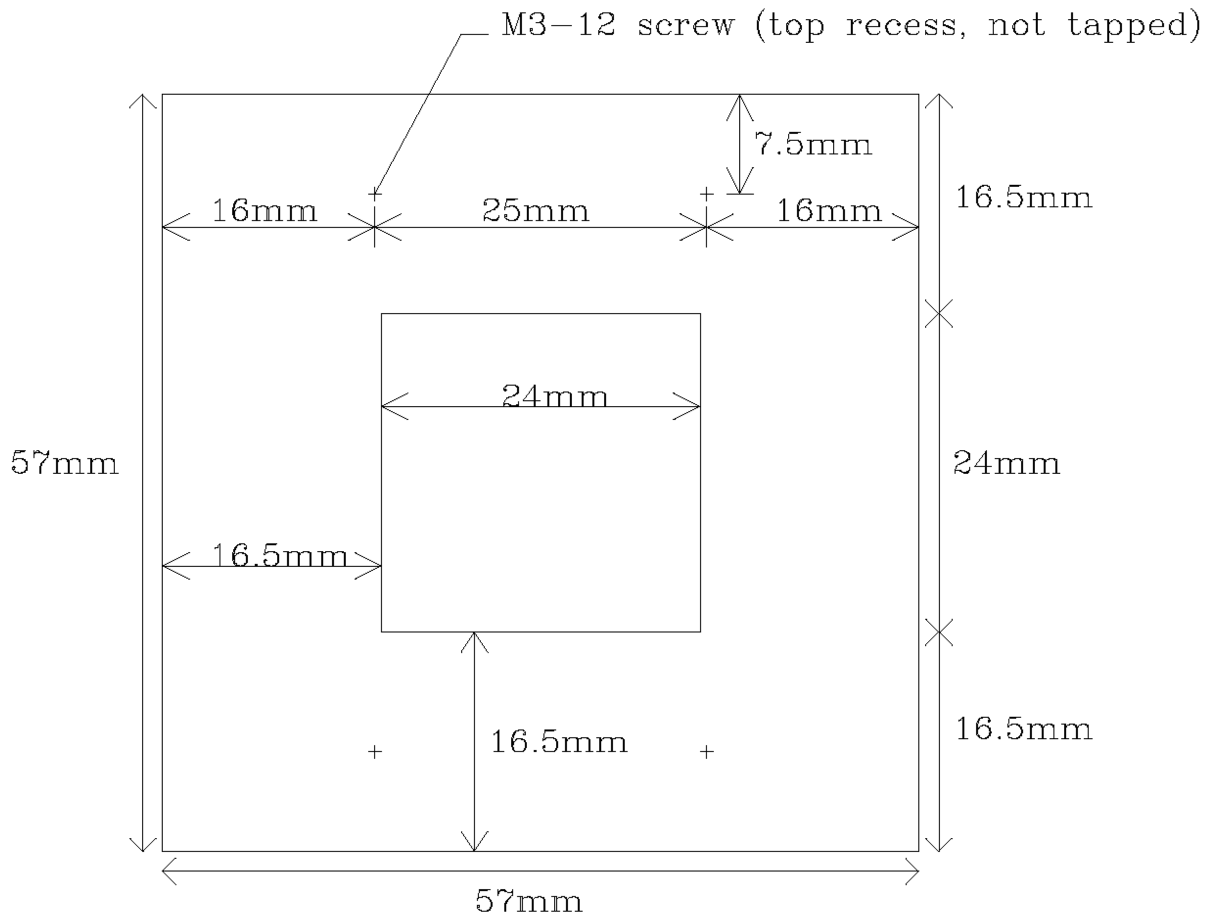

Figure E.2: Top of fixture Design.